“CFD ANALYSIS OF COMPRESSOR BLADE CASCADE”

A DISSERTATION

SUBMITTED IN PARTIAL FULFILLMENT OF THE REQUIREMENTS FOR THE AWARD OF THE DEGREE OF

MASTER OF TECHNOLOGY

IN

THERMAL ENGINEERING

Submitted by:

RAVI KUMAR VERMA

(Roll No. 2K16/THE/18)

Under the supervision of

DR. SAMSHER

PROFESSOR

DEPARTMENT OF MECHANICAL ENGINEERING

DELHI TECHNOLOGICAL UNIVERSITY

(Formerly Delhi College of Engineering)

Bawana Road, Delhi-110042

JULY, 2018

DELHI TECHNOLOGICAL UNIVERSITY

(Formerly Delhi College of Engineering)

Bawana Road, Delhi-110042

CANDIDATE'S DECLARATION

I, RAVI KUMAR VERMA, Roll No. 2K16/THE/18 student of M.Tech (Thermal Engineering), hereby declare that the project Dissertation titled "CFD ANALYSIS OF AXIAL COMPRESSOR BLADE CASCADE" which is submitted by me to the Department of Mechanical Engineering, Delhi Technological University, Delhi in partial fulfillment of the requirement for the award of the degree of Master of Technology, is original and not copied from any source without proper citation. This work has not previously formed the basis for the award of any Degree, Diploma Associateship, Fellowship or other similar title or recognition.

Place: Delhi **RAVI KUMAR VERMA**

Date:

DEPARTMENT OF MECHANICAL ENGINEERING

DELHI TECHNOLOGICAL UNIVERSITY

(Formerly Delhi College of Engineering)

Bawana Road, Delhi-110042

CERTIFICATE

I hereby certify that the project Dissertation titled "CFD ANALYSIS OF AXIAL COMPRESSOR BLADE CASCADE" which is being submitted by RAVI KUMAR VERMA, Roll No. 2K16/THE/18, Department of Mechanical Engineering, Delhi Technological University, Delhi in partial fulfillment of the requirement for the award of degree of Master of Technology, is a record of the project work carried out by the student under my supervision. To the best of my knowledge this work has not been submitted in part or full for any Degree or Diploma to this University or elsewhere.

Place: Delhi **(DR. SAMSHER)**

Date: **SUPERVISOR**

PROFESSOR

DEPARTMENT OF MECHANICAL ENGINEERING

ACKNOWLEDGEMENT

Any accomplishment is a result of positivity of thoughts and efforts. It is important here to appreciate contribution, encouragement and support from persons who stood as 'Light House' throughout the voyage.

I wish to express my sincere gratitude for my project supervisor and mentor, DR. SAMSHER, Professor, Department of Mechanical Engineering, Delhi Technological University (Delhi). It was a golden opportunity to work under his kind supervision. His scholastic guidance and sagacious suggestions helped me to complete the project.

I wish to thank Dr. Vipin, Head, Department of Mechanical Engineering, Delhi Technological University (Delhi), for constantly motivating and providing able guidance.

I am also thankful to the staff of Department of Mechanical Engineering for their continual support and cooperation.

Finally, but importantly, I would like to express my heartfelt thanks to my beloved family and friends who have endured the long working hours and whose motivation kept me going.

RAVI KUMAR VERMA

(Roll No. 2K16/THE/18)

M.Tech. (Thermal Engineering)

Delhi Technological University, Delhi, India

ABSTRACT

Efficiency is the key design parameter in today's aeronautical engine industry. In axial compressor blades, the leading edge is the crucial part its geometry and the way it interacts with the incoming wakes has decisive effects on the boundary layer characters and therefore on the loss.

This work aims to investigate the effect of the leading edge geometry on the performances of a compressor stage. In particular, the interaction between the leading edge and the wake coming from the upstream blade row should be investigated. Gaining some understanding of the physics of this complex process and, more in general, of the behavior of the flow around the leading edge could lead to the design of optimized geometries with improved performances.

In this work, three geometries have been tested: a high wedge angle blade (32°) with circular leading edge and two low wedge angle blades (15°) with circular and elliptic (3:1 axes ratio) leading edges, representative of real engine blades. Numerical investigations in a low speed axial compressor have been undertaken, using JAVAFOIL AND ANSYS [CFD] software.

The reported results show that the leading edge geometry in order to avoid the leading edge separation bubble to appear, may lead to significant loss reduction. A high wedge angle and an elliptic shaped leading edge proved to be able to achieve this. A comparison with the test case with circular leading edge and low wedge angle showed a 25% drop in the loss coefficient. This result gives an idea of the improvement offered by the research on compressor leading edges.

TABLE OF CONTENTS

LIST OF FIGURES

LIST OF ABBREVIATION

a	[mm] Short semi-axis
b	[mm] Long semi-axis
C_f	[-] Friction coefficient
C_p	[-] Pressure coefficient
C_{dyn}	[-] Dynamic head calibration coefficient
C_{stage}	[-] Stagnation calibration coefficient
C_{yaw}	[-] Yaw calibration coefficient
E	[V] Voltage
H	[-] Shape factor
K	[1/m] Curvature
K	[-] Constant
ℓ	[m] Length
m	[-] Arc length coordinate (Javafoil)
n	[m] Normal coordinate
OHR	[-] Over heat ratio
p	[Pa] Pressure
P_{in}	[Pa] Inlet pressure
P_{out}	[Pa] Outlet pressure

P_{total}	[Pa] Total pressure
P_{mixed}	[Pa] Mixed averaged pressure
P_{ref}	[Pa] Reference pressure
r	[m] Radial coordinate
R	[Ω] Resistance
Re	[-] Reynolds number
S1	[-] Inlet slope (Javafoil)
T	[°C] Temperature
U	[m/s] Blade velocity
u	[m/s] Fluid velocity
v_x	[m/s] Axial velocity
v_θ	[m/s] Tangential velocity
x	[m] x-coordinate, axis
y	[m] y-coordinate, axis
Y_p	[-] Loss coefficient
z	[m] z-coordinate, axis (Javafoil)
α	[°] Flow angle (absolute)
α_w	[°] Flow angle with wake (absolute)
β	[°] Flow angle (Relative)

β_w	[°] Flow angle with wake (relative)
$\emptyset$	[-] Flow coefficient
θ	[°] Tangential angle
θ	[mm] Momentum thickness
θ_{TE}	[mm] Trailing edge momentum thickness
θ_0	[mm] Leading edge momentum thickness
ρ	[kg/m^3] Density
ρ	[Ω.m] Resistivity

CHAPTER 1

INTRODUCTION

Study compressor leading edges and their interaction with the incoming wakes is an important part of compressor cascade analysis. This research topic aims to gain some understanding about the physics of the interaction between wakes and boundary layers and about the influence that specifically tuned leading edge geometry can have on the character of the boundary layer and on the performance of a compressor aerofoil. A large potential of improvement is believed to lay behind this topic. Optimized leading edge geometries may lead to significant improvements in the performance, raising the efficiency of compressor stages of aeronautical engines.

1.1 INTENT OF STUDY

First goal of the work is to modify the shape of an existing blade and obtain two new profiles with new leading edge geometry. These must be representative of real engine blades. A blade with circular leading edge and one with elliptic leading edge have to be designed. Using the computational fluid dynamics (CFD) package, a two dimensional, steady analysis must be performed on the airfoil at mid-height of the designed three dimensional blades. The experiment should point to the measurement of loss: time averaged Y_p measurements and trailing edge momentum thickness measurements are wanted. Final goal is to investigate the boundary layer to gain some understanding on the interaction between wakes and leading edge. The mechanisms of losses related with the wake interaction and the effect of the different geometries on it are the focus of this analysis.

1.2 AXIAL FLOW COMPRESSOR

The axial flow compressor is one in which the flow enters the compressor in an axial direction (parallel with the axis of rotation), and exits from the gas turbine. The accelerating the fluid and then diffusing it to obtain a pressure increase.

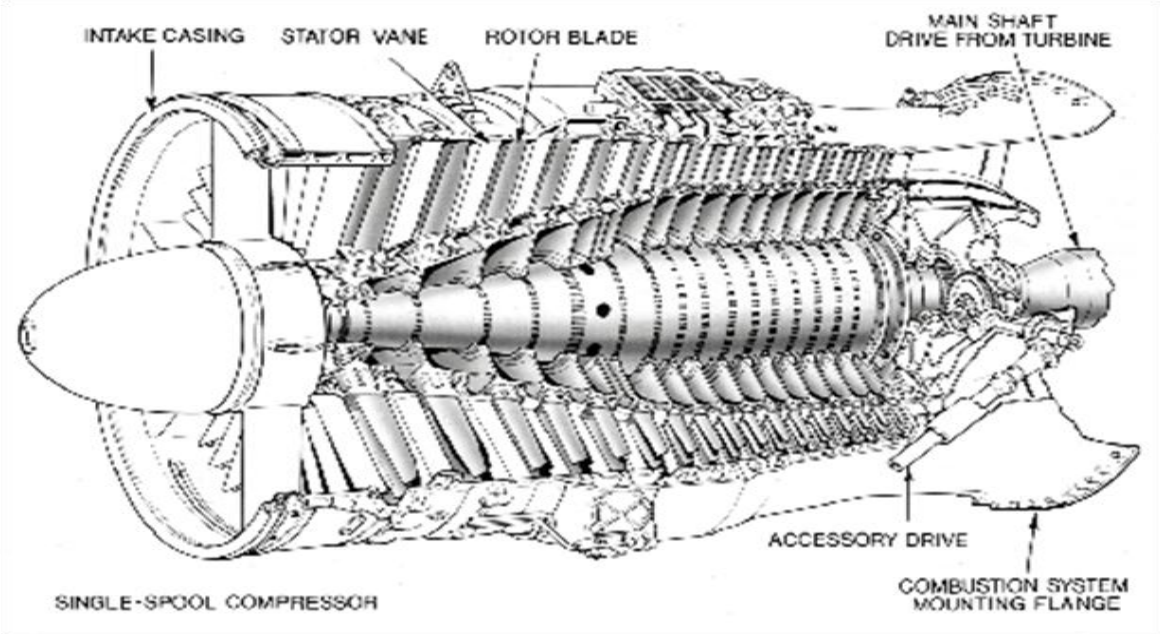

Figure 1.1 Schematics diagram of axial blade compressor.

1.3 BLADE NOMENCLATURE

There are three types of angle in compressor cascade

- Camber angle
- Blade angle
- Air angles

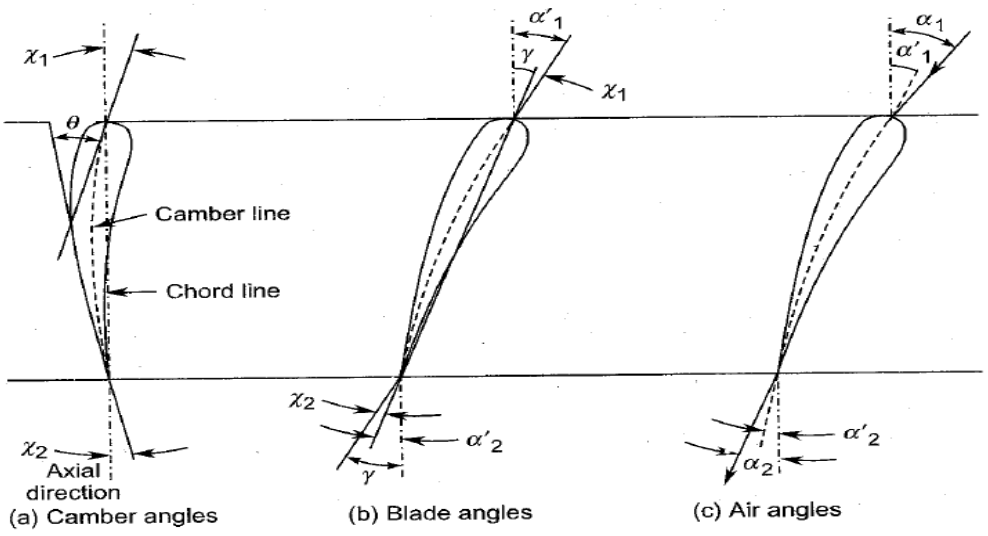

Figure 1.2 Camber, blade and air angle [5]

The camber angle is defined by

$$\theta = \chi_1 + \chi_2 = \alpha'_1 - \alpha'_2 \ldots\ldots\ldots\ldots\ldots\ldots\ldots\ldots\ldots\ldots Eq - 1.1$$

$$\alpha'_1 = \chi_1 + \gamma \ldots\ldots\ldots\ldots\ldots\ldots\ldots\ldots\ldots\ldots\ldots\ldots\ldots Eq - 1.2$$

$$\alpha'_2 = -(\chi_1 - \gamma) \ldots\ldots\ldots\ldots\ldots\ldots\ldots\ldots\ldots\ldots\ldots\ldots Eq - 1.3$$

The difference between the air and the blade angles at the entry is known as the incidence angle.

$$i = \alpha_1 - \alpha'_1 \ldots\ldots\ldots\ldots\ldots\ldots\ldots\ldots\ldots\ldots\ldots\ldots\ldots Eq - 1.4$$

This angle can be positive or negative.

The deviation angle (δ) for the compressor cascade is defined as the difference of the air angle and the blade angle at exit.

$$\delta = \alpha_2 - \alpha'_2 \ldots\ldots\ldots\ldots\ldots\ldots\ldots\ldots\ldots\ldots\ldots\ldots\ldots Eq - 1.5$$

Fluid deflection through the blades is defined as

$$\mathcal{E} = \alpha_1 - \alpha_2 \ldots\ldots\ldots\ldots\ldots\ldots\ldots\ldots\ldots\ldots\ldots\ldots\ldots Eq - 1.6$$

$$\mathcal{E} = \theta + i - \delta \ldots\ldots\ldots\ldots\ldots\ldots\ldots\ldots\ldots\ldots\ldots\ldots\ldots Eq - 1.7$$

1.4 AXIAL FLOW COMPRESSOR LOSS MECHANISM

1.4.1 Viscous losses

Viscous losses are that accounts the effect of viscosity property of fluid during flow over blade surface.

- Profile losses: - This loss associated with the growth of boundary layer on the bon account of the profile or nature of the airfoil cross-sections blade surface. Separation of boundary layer occurs when the adverse pressure gradient on the surface or surfaces becomes too steep; this increases the profile losses. The pattern of the boundary layer growth and its separation depend on the geometries of the blade and the flow. Positive and negative stall losses occur on account of increased positive or negative incidences respectively.

- Annulus losses: - in stationary blade rows, a loss of energy occurs due to growth of the boundary layer on the end walls, this also occurs in the rotating row of blades but the flow on the end walls, in this case, is subjected to effects associated with the rotation of the cascade.

- Endwall losses: - boundary layer effects in the corner (junction between the blade surface and the casing/hub)

1.4.2 Three Dimensional Effect Losses

- Secondary flows - The loss occurs in the region near the end walls owing to the presence of unwanted circulatory or cross flows. such secondary flows develop on account of turning of the through the blade channel in the presence of annuls wall boundary layers. Figure (1.3) depicts the pressure gradients across a blade channel and the secondary and trailing vortices.

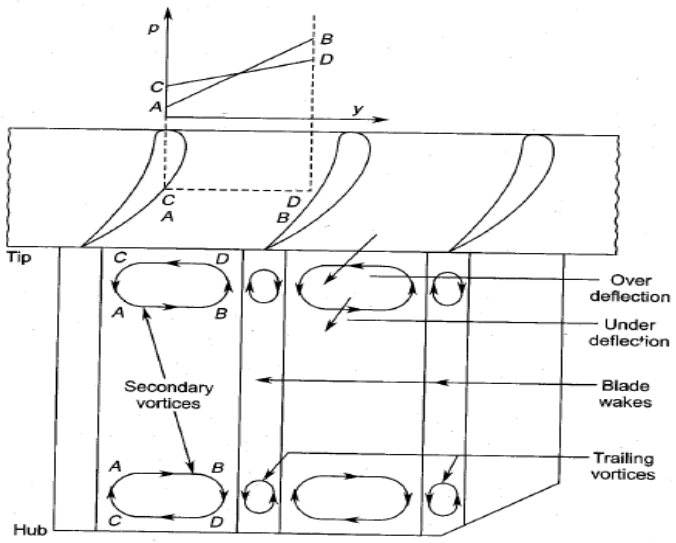

Figure 1.3 secondary flow in cascade blade [1]

- Tip leakage flows: flow from pressure surface to suction surface at the blade tip

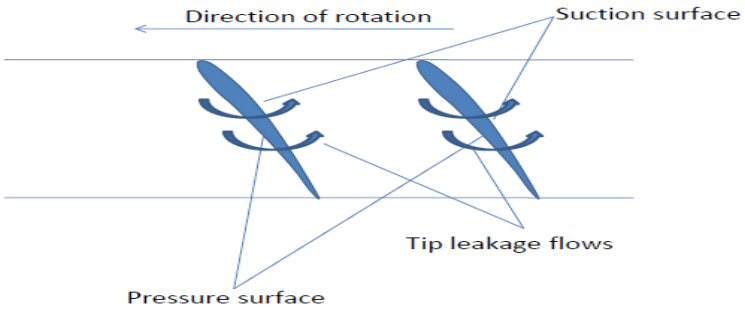

Figure 1.4 Tip leakage flow in cascade blade [1]

- Mixing losses: Interaction of the flow from the rotor with the succeeding stator, stator wakes with the succeeding rotor etc.

- Includes the effect of wakes interaction with the blades. Estimating the losses crucial designing loss control mechanisms. However isolating these losses not easy and often done through empirical correlations. Total losses in a compressor are the sum of the above losses.

Total Loss = Profile + End Wall

$$\omega_{TOTAL} = \omega_P + \omega_{EW} \ldots\ldots\ldots\ldots\ldots\ldots Eqn - 1.8$$

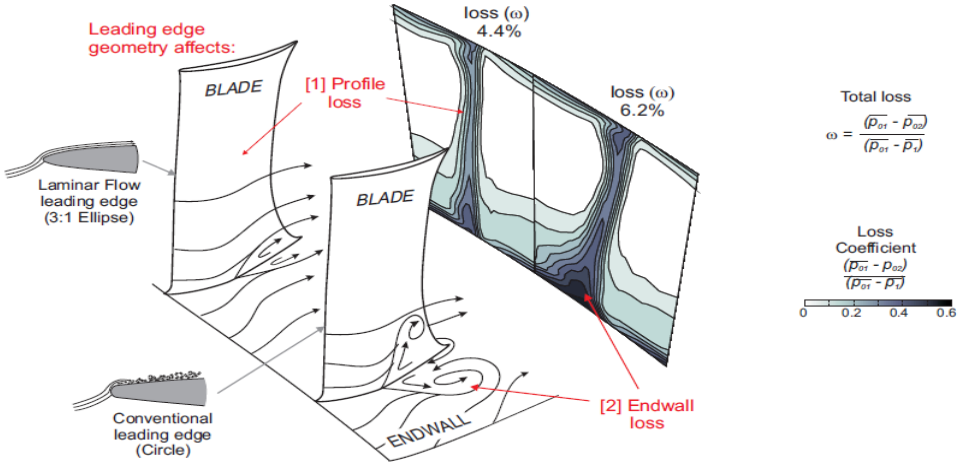

Figure 1.6: The benefit of laminar flow leading edges: Schematic of surface limiting streamlines and plots of stagnation pressure deficit measured downstream.[5]

1.5 EFFECT OF LOSSES IN COMPRESSOR BLADES

- The annulus-wall region accounts for up to 50 % of the total losses.
- The leakage vortex interacts with the blade boundary layer, casing boundary layer and the secondary flows.
- There is a large turbulence production due to mixing in this zone.
- The presence of a shock wave increases the complexity.
- In the hub region, there are corner stalls, which may increase the effective blockage.

1.5.1 Correlation For Profile Losses

- The correlation for profile loss is developed using test data on linear cascades.
- One major issue in development of a correlation is the choice of independent variables.

- Cascade tests can not be carried out with a variation of one parameter.
- For instance, if the effect of Reynolds number is being measured, almost invariably the Mach number or the aspect ratio of the cascade is being simultaneously altered.

1.5.2 Non-dimensional Variables affecting Profile Losses

- The correlation evolved is based on the analysis of over 100 specific cascade tests and on comparisons with a wide variety of published information.
- All losses in are related on a basis of velocity coefficients and are dependent on the following parameters :
- (1) Reynolds number *(Re) (based on outlet velocity)*
- *(2) Aspect ratio (blade height/chord length ratio);*
- *(3) Blade angles and passage geometry;*
- (4) Pitch to chord length ratio;
- (5) Mach number *(Mu);*
- (6) Incidence.

1.5.3 General Practice

- The profile loss correlation is presented in the form of a basic loss correlation for incompressible flow conditions.
- The basic correlation itself are derived originally from low speed tests where it could be assumed that the Ma effects could be ignored.
- The correlation mainly involves a variation in *Blade angles, passage geometry* and *Pitch to chord length ratio* only

- Multiplying correction factors are presented to consider the variation of other parameters.

1.5.4 Effect of Reynolds number

- Re will have a pronounced effect on profile loss.
- Typically in the range of Re between 2 x $l0^4$ and 2 x $l0^5$ the loss will be halved.
- A general prediction method for use in steam turbine analysis requires that the effect of Re should be predictable up to values of Re, equal to about 4 x $l0^6$.
- This range is obtained at the inlet of modern high pressure (h.p.) cylinders.
- Thus any correlation of cascade data which neglects the Reynolds number of test is of little value.

1.6 CASCADE AND TYPES OF CASCADING

A row of blades representing the blade ring of an actual turbomachine is called cascade, grid, lattice, or mesh of blades.

Cascade of blades are of two types:

a. Linear.

b. Annular.

A linear cascade comprises a row of blades corresponding to the sectional profile at a given radial location along the blade height and spaced at a pitch corresponding to that radius in the actual machine.

An annular cascade comprises a row of blades representing the actual rotor or stator blade row in the actual machine. The test blade row remains stationary.

The cascade test should take into account the geometric and aerodynamic similarities with respect to the actual blades / blade sections.

Cascade tests provide a quick and cost effective way of assessing the **Performance of individual blade sections;** Owing to complex 3D flow in the actual turbomachines, the data from linear cascades may not be directly correlated, but it still provides good information to the designer in selecting optimum blade profiles.

1.6.1 Cascade Testing

To obtain truly two-dimensional flow, the cascade should be of infinite extent. Of necessity cascades must be limited in size, and careful design is needed to ensure that at least the central regions (where flow measurements are made) operate with approximately two-dimensional flow.

For high hub-tip radius ratio machines, the radial velocities are negligible and, to a close approximation, the flow may be described as two dimensional. The flow in a cascade is then a reasonable model of the flow in the machine.

In low hub-tip radius ratio machines, the blades will normally have an appreciable amount of twist along the height, depending upon the "vortex design" chosen. However, the data obtained from the two-dimensional cascades can still be of value to the

1.7 MODELLING OF CASCADE BLADE

There are two basic methodologies to model cascade blades in turbo machinery;

I. Experimental

II. Numerical

1.7.1 Experimental Cascade Modelling

Cascade of blade is constructed by assembling a number of blades of a given shape and sizes at the required pitch(S) and stagger angle (γ). The assembly is then fixed in wind tunnel. Air at slight pressure and near ambient temperature is blown over the cascade of blades to simulate the flow over an actual blade row in a turbomachines. The test section of the wind tunnel has a rectangular cross section of the cascade inlet. It

provides independent boundary layer adjustment options of all four side walls. The upper and lower boundary layers are sucked to obtain a periodic flow in the compressor cascade. By monitoring the static pressure in the pitchwise direction in the cascade inlet plane the periodicity is ensured. A rake with pitot tubes for total pressure measurement, Conrad angle probes for outflow angle determination, and a static pressure probe is used for the wake measurements.

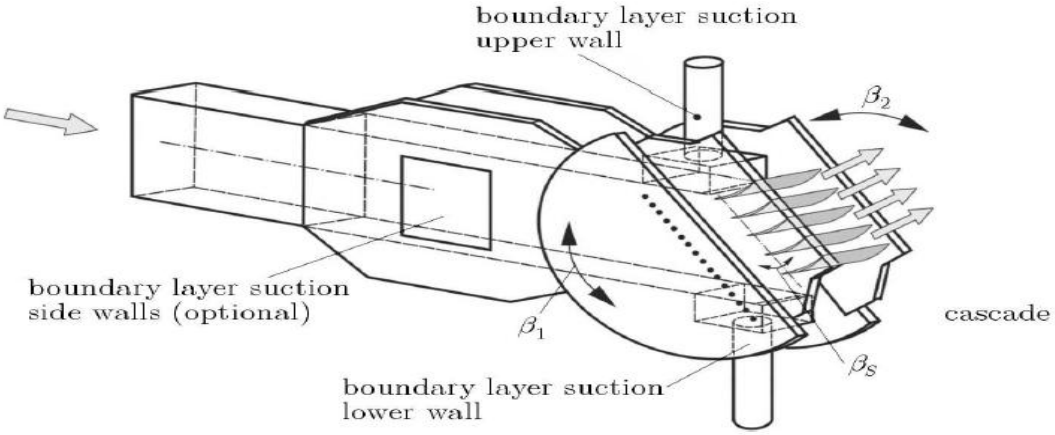

Figure 1.5 Sketch of Test Section [7]

1.7.2 Numerical Cascade Modelling

In the cases where the experimental techniques for the problems are not appropriate to be applied, the engineers use the CFD tools to obtain information about the fluid flow problems and the flow parameters like pressure, velocity and temperature. Computational Fluid Dynamics (CFD) deals with the numerical solution of a set of differential equations defining a fluid flow and related phenomena to obtain specific information of the flow field. Although the area is still developing and new techniques are emerging, satisfactory results are obtained to engineering problems.

1.7.3 Mathematical Model

The mathematical model is the starting point of any numerical method, i.e. the set of Partial differential equations and boundary conditions. The sets of equations are

chosen for target application (inviscid, incompressible, turbulent, two or three dimensional).

Using tensor notation in Cartesian coordinates, continuity equation is

$$\frac{\partial u}{\partial x} = S_m \ldots\ldots\ldots\ldots\ldots\ldots\ldots\ldots\ldots\ldots\ldots\ldots\ldots\ldots\ldots\ldots Eq - 1.9$$

Conservation of momentum (Navier-Stokes Equations) for incompressible flow is

$$\rho \frac{\partial u_i}{\partial t} + \rho \frac{\partial (u_f u_i)}{\partial x_i} = -\frac{\partial p}{\partial x_i} + \frac{\partial \left(2\mu s_{ij}\right)}{\partial x_i} + \rho g_i + F_i \ldots\ldots\ldots Eq - 1.10$$

where F_i is external body force and s_{ij} is the stress tensor which is given by

$$S_{ij} = \frac{1}{2}\left(\frac{\partial u_i}{\partial x_j} + \frac{\partial u_j}{\partial x_i}\right) \ldots\ldots\ldots\ldots\ldots\ldots\ldots\ldots\ldots\ldots\ldots Eq - 1.11$$

1.7.3.1 Spalart-Allmaras One Equation Model

In turbulence models that employ the Boussinesq approach, the central issue is how the eddy viscosity is computed. The model proposed by Spalart and Allmaras solves a transport equation for a quantity that is a modified form of the turbulent kinematic viscosity. The model was designed specifically for aerospace applications involving wall-bounded flows and has been shown to give good results for boundary layers subjected to adverse pressure gradients [2]. This is why the model is selected in the study for the aerodynamic analysis of the blade cascades.

The eddy viscosity equation is given by

$$\frac{\partial \tilde{\upsilon}}{\partial t} + \frac{\partial \tilde{\upsilon}}{\partial x_j} = c_{b1} s \tilde{\upsilon} - c_{w1} f_w \left(\frac{\tilde{\upsilon}}{d}\right)^2 + \frac{1}{\sigma}\frac{\partial}{\partial x_k}\left[(\upsilon + \tilde{\upsilon})\frac{\partial \tilde{\upsilon}}{\partial x_k}\right] + \frac{c_{b1}}{\sigma}\frac{\partial \tilde{\upsilon}}{\partial x_k}\frac{\partial \tilde{\upsilon}}{\partial x_k} \ldots Eq - 1.12$$

in Eqn 1.12 the first term on the right hand side is the production of turbulent viscosity and the second term is the destruction of turbulent viscosity that occurs in the near wall

region due to wall blocking and viscous damping. Note that since the turbulent kinetic energy (k) is not calculated in Spalart-Allmaras model, the last term in Eq. (1.12) is ignored when estimating Reynolds stresses.

The kinematic eddy viscosity (υ_T) is computed from

$$\upsilon_T = \tilde{\upsilon}.f_{v1} \ldots\ldots\ldots\ldots\ldots\ldots\ldots\ldots\ldots\ldots\ldots\ldots\ldots\ldots\ldots\ldots\ldots\ldots Eq-1.13$$

So, including both the rotation and strain tensors reduces the production of eddy viscosity and consequently reduces the eddy viscosity itself in regions where the measure of vorticity exceeds that of strain rate. One such example can be found in vertical flows, i.e., flow near the core of a vortex subjected to a pure rotation where turbulence is known to be suppressed. Including both the rotation and strain tensors more correctly accounts for the effects of rotation on turbulence. The option including the rotation tensor only tends to over predict the production of eddy viscosity and hence over predicts the eddy viscosity itself in certain circumstances

1.7.3.2 Standard k-ε Model

As it is mentioned before, the three forms of k- ε models have similar forms for transport equations of k and ε. These models differ in how the turbulent viscosity is calculated, the turbulent Prandtl numbers governing the turbulent diffusion of k and ε and the generation and the destruction terms in ε equation. The Standard k- ε model is as follows:

Transport equation for turbulence kinetic energy

$$\frac{\partial k}{\partial t} + U_j \frac{\partial k}{\partial x_j} = G_k + G_b - \varepsilon + \frac{\partial}{\partial x_k}\left[(\upsilon + \upsilon_T/\sigma_k)\frac{\partial k}{\partial x_j}\right] \ldots\ldots\ldots\ldots Eq-1.14$$

G_k is the generation of turbulent kinetic energy due to mean velocity gradients and isdefined as

$$G_k = u'_i u'_j \frac{\partial u_j}{\partial x_i} \ldots\ldots\ldots\ldots\ldots\ldots\ldots\ldots\ldots\ldots\ldots\ldots\ldots\ldots\ldots\ldots Eq-1.15$$

To evaluate in a manner consistent with Boussinesq hypothesis,

$$G_k = \upsilon_T s^2 \ldots\ldots\ldots\ldots\ldots\ldots\ldots\ldots\ldots\ldots\ldots\ldots\ldots\ldots\ldots\ldots\ldots\ldots\ldots Eq - 1.16$$

where S is the modulus of mean rate of strain tensor and is defined as in Eq (1.16).

G_b is the generation of turbulence kinetic energy due to buoyancy and is given by

$$G_b = \beta g_i \frac{\upsilon_T}{Pr} \frac{\partial T}{\partial x_i} \ldots\ldots\ldots\ldots\ldots\ldots\ldots\ldots\ldots\ldots\ldots\ldots\ldots\ldots\ldots\ldots Eq - 1.17$$

where Pr is turbulent Prandtl number and g_i is the component of gravitational acceleration in the ith direction and β is the coefficient of thermal expansion. For the standard model, the value of Pr is 0.85 and β is given by

$$\beta = -\frac{1}{\rho}\left(\frac{\partial \rho}{\partial T}\right)_p \ldots\ldots\ldots\ldots\ldots\ldots\ldots\ldots\ldots\ldots\ldots\ldots\ldots\ldots\ldots\ldots\ldots Eq - 1.18$$

The transport equation for turbulence dissipation rate (ε)

$$\frac{\partial k\varepsilon}{\partial t} + U_j \frac{\partial k\varepsilon}{\partial x_j} = \frac{\partial}{\partial x_j}\left[(\upsilon + \upsilon_T/\sigma_\varepsilon)\frac{\partial \varepsilon}{\partial x_j}\right] + C_{1\varepsilon}\frac{\varepsilon}{k}(G_k + C_{3\varepsilon}G_b) - C_{1\varepsilon}\frac{\varepsilon^2}{k} \ldots Eq - 1.19$$

The eddy viscosity is computed by combining k and ε as follows

$$\upsilon_T = C_\mu \frac{k^2}{\varepsilon} \ldots\ldots\ldots\ldots\ldots\ldots\ldots\ldots\ldots\ldots\ldots\ldots\ldots\ldots\ldots\ldots\ldots\ldots\ldots\ldots Eq - 1.20$$

The constant $C_{3\varepsilon}$ is the degree to which ε is affected by buoyancy and is given by

$$C_{3\varepsilon} = \tanh\left|\frac{v}{u}\right| \ldots\ldots\ldots\ldots\ldots\ldots\ldots\ldots\ldots\ldots\ldots\ldots\ldots\ldots\ldots\ldots\ldots Eq - 1.21$$

where v is the component of flow velocity parallel to gravitational vector and u is the component of flow velocity perpendicular to gravitational vector.

1.7.4 Overview of the FLUENT CFD Program

FLUENT is a state-of-the-art computer program for modeling fluid flow and heat transfer in complex geometries, using Finite Volume Method (FVM). FLUENT is written in the C computer language and makes full use of the flexibility and power offered by the language. Consequently, true dynamic memory allocation, efficient data structures, and flexible solver control are all made possible.

1.7.5 Program Structure

FLUENT package includes the following products:

- FLUENT, the solver.
- Pre PDF, the preprocessor for modeling non-premixed combustion in FLUENT.
- GAMBIT, the preprocessor for geometry modeling and mesh generation.
- T Grid, an additional preprocessor that can generate volume meshes from existing boundary meshes.
- Filters (translators) for import of surface and volume meshes from CAD/CAE packages such as ANSYS, I-DEAS, NASTRAN, PATRAN, and others.

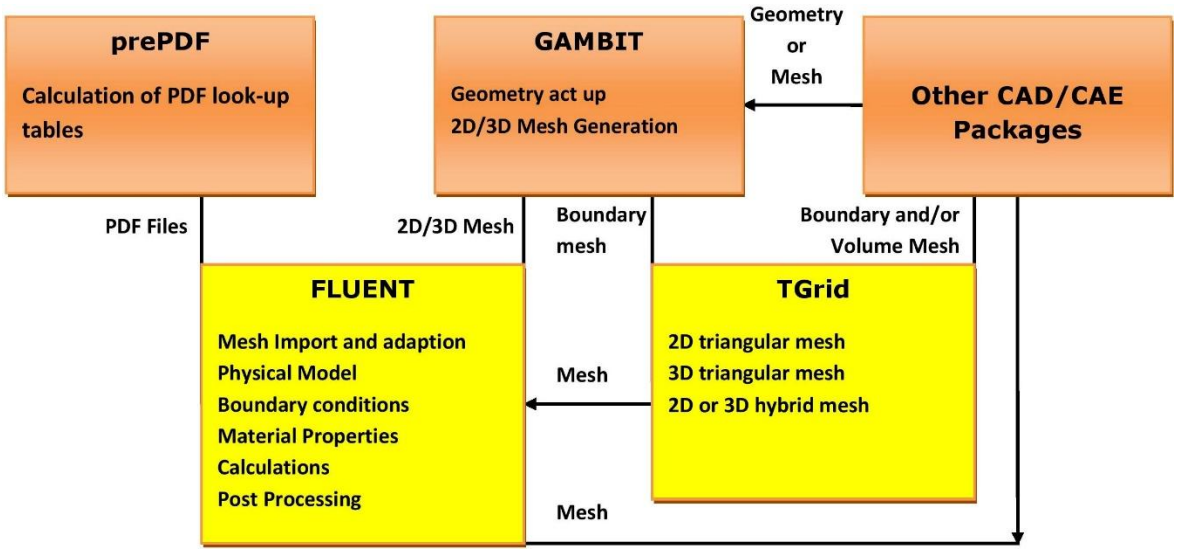

Figure 1.7 Basic Program Structure

1.7.6 Boundary Conditions

Boundary conditions specify the flow and thermal variables on the boundaries of the physical model. They are, therefore critical component of CFD simulations and it is important that they are specified appropriately. The boundary types that are available in FLUENT as follows:

- Flow inlet and exit boundaries: pressure inlet, velocity inlet, mass flow inlet, inlet vent, intake fan, pressure outlet, pressure far-field, outflow, outlet vent, exhaust fan
- Wall, repeating, and pole boundaries: wall, symmetry, periodic, axis
- Internal cell zones: fluid, solid (porous is a type of fluid zone)
- Internal face boundaries: fan, radiator, porous jump, wall, interior most commonly used boundary condition types will be presented briefly.

1.7.6.1 Flow Inlet/Exit Boundary Conditions

FLUENT provides 10 types of boundary zone types for the specification of flow inlets and exits.

- Velocity inlet boundary conditions are used to define the velocity and scalar properties of the flow at inlet boundaries.
- Pressure inlet boundary conditions are used to define the total pressure and other scalar quantities at flow inlets.
- Mass flow inlet boundary conditions are used in compressible flows to prescribe a mass flow rate at an inlet. It is not necessary to use mass flow inlets in incompressible flows because when density is constant, velocity inlet boundary conditions will fix the mass flow.
- Pressure outlet boundary conditions are used to define the static pressure at flow outlets (and also other scalar variables, in case of backflow). The use of a pressure

outlet boundary condition instead of an outflow condition often results in a better rate of convergence when backflow occurs during iteration.

- Pressure far-field boundary conditions are used to model a free-stream compressible flow at infinity, with free-stream Mach number and static conditions specified. This boundary type is available only for compressible flows.

- Outflow boundary conditions are used to model flow exits where the details of the flow velocity and pressure are not known prior to solution of the flow problem. They are appropriate where the exit flow is close to a fully developed condition, as the outflow boundary condition assumes a zero normal gradient for all flow variables except pressure. They are not appropriate for compressible flow calculations.

- Inlet vent boundary conditions are used to model an inlet vent with a specified loss coefficient, flow direction, and ambient (inlet) total pressure and temperature.

- Intake fan boundary conditions are used to model an external intake fan with a specified pressure jump, flow direction, and ambient (intake) total pressure and temperature.

- Outlet vent boundary conditions are used to model an outlet vent with a specified loss coefficient and ambient (discharge) static pressure and temperature.

- Exhaust fan boundary conditions are used to model an external exhaust fan with a specified pressure jump and ambient (discharge) static pressure.

1.7.6.2 Wall Boundary Conditions

Wall boundary conditions are used to bound fluid and solid regions. In viscous flows, the no-slip boundary condition is enforced at walls by default, but one can specify a tangential velocity component in terms of the translational or rotational motion of the wall boundary, or model a ``slip'' wall by specifying shear. The shear stress and heat transfer between the fluid and wall are computed based on the flow details in the local flow field.

1.7.6.3 Symmetry Boundary Conditions

Symmetry boundary conditions are used when the physical geometry of interest and the expected pattern of the flow/thermal solution have mirror symmetry. They can also be used to model zero-shear slip walls in viscous flows. Symmetry boundaries are used to reduce the extent of the computational model to a symmetric subsection of the overall physical system.

1.7.6.4 Periodic Boundary Conditions

Periodic boundary conditions are used when the physical geometry of interest and the expected pattern of the flow/thermal solution have a periodically repeating nature.

Two types of periodic conditions are available in FLUENT.

- The first type does not allow a pressure drop across the periodic planes.
- The second type allows a pressure drop to occur across translationally periodic boundaries, enabling you to model ``fully-developed" periodic flow.

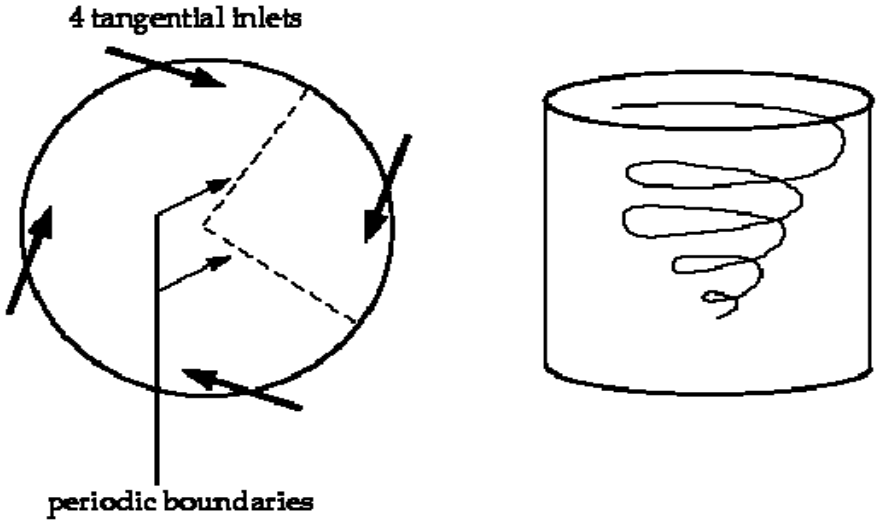

Figure 1.8 Rotationally periodic BCs, swirling flow in a cylindrical vessel

CHAPTER 2

LITERATURE REVIEW

2.1 FLOWS AROUND THE LEADING EDGE OF A COMPRESSOR BLADE

2.1.1 Suction Spike and Separation Bubble

Cumpty N.A [1990] [10] The flow around the leading edge of a compressor blade is described in The flow impinges on the leading edge at the stagnation point and then splits and flows onto the pressure or suction surface.

Because of the curvature of the leading edge, the flow strongly accelerates as it goes around it; then it decelerates when it meets the relatively flat surface. The suction and pressure surfaces are not flat, but their curvature is much smaller than that of the leading edge. The leading edge can therefore be seen as a circle and two straight lines tangent to it. The two tangent points are the wedge points.

The rapid acceleration and deceleration around the leading edge causes a peak in the cp distribution. The steep deceleration on the downward side of the spike can cause the flow to separate, to undergo transition and to reattach as a turbulent boundary layer, forming a separation bubble.

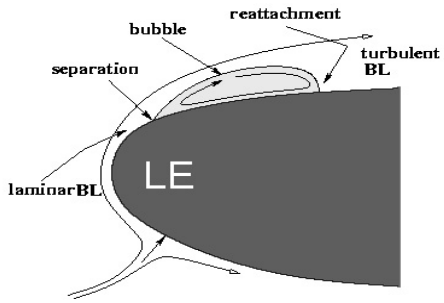

Figure 2.1: Leading edge separation bubble

Aresna A.V et al. [1980] [11] characteristics of the separation bubble and the mechanisms of transition and reattachment are shortly reviewed here as explained. The separated laminar boundary layer gives a laminar shear flow, which is very unstable and goes into transition. A turbulent shear layer originates; this entrains fluid from the external stream and grows rapidly. As a result, the turbulent

layer bends toward the wall and reattaches forming the bubble. Since the separated region cannot support any pressure gradient, a small plateau of static pressure (or at least a kink) can be observed in the distribution of the non dimensional pressure coefficient cp, defined as follows.

$$Cp = \frac{\mathrm{P_{tot,in}} - \mathrm{P}}{\mathrm{P_{tot,in}} - \mathrm{P_{in}}} \ldots\ldots\ldots\ldots\ldots\ldots\ldots\ldots\ldots\ldots\ldots\ldots\ldots\ldots. \mathrm{Eq.\,2.1}$$

2.1.2 Circle Versus Ellipse

Walreavens R.E. et al.[1995] [12] The shape of the leading edge is a key parameter to influence the size and the characteristics of the separation bubble. where a flat plate with different leading edge geometries has been studied. Similarly to this work, circular and elliptic leading edges have been tested, and the elliptic one has proved better performances in reducing the size of the bubble and making the reattachment possible at higher incidence.

An attempt to analytically explain the benefits of an elliptic leading edge in comparison to a circular one is presented here. As described in the previous paragraph, the curvature of the leading edge forces the flow to accelerate. This can be understood considering the following momentum conservation equation.

$$\frac{\partial p}{\partial n} = K.\rho.u^2 \ldots\ldots\ldots\ldots\ldots\ldots\ldots\ldots\ldots\ldots\ldots\ldots\ldots\ldots \mathrm{Eq.\,2.2}$$

With K being the local streamline curvature and having the dimension $\frac{1}{l}$. Regions of high convex curvature of the streamlines are associated with low pressure and high velocity. Furthermore, the radial pressure gradient is proportional to the curvature.

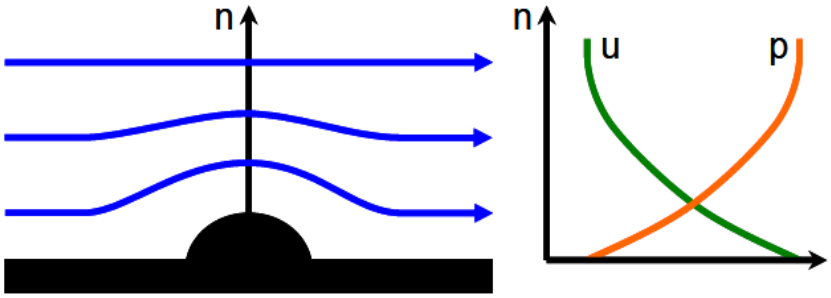

Figure 2.2: Streamline curvature

Equation Eq. 2.2 shows also that the sudden drop in curvature occurring at the wedge point causes a drop in the radial pressure gradient and a steep deceleration. This strong diffusion can eventually cause the separation. It is now clear that a large discontinuity in curvature should be avoided in order to prevent the separation bubble to appear at the wedge point. A circle is a geometric figure characterized by a constant curvature being equal to$1/r$. A circular leading edge is therefore a region of constant curvature followed by a flat region. At the wedge point, the curvature suddenly drops to zero.

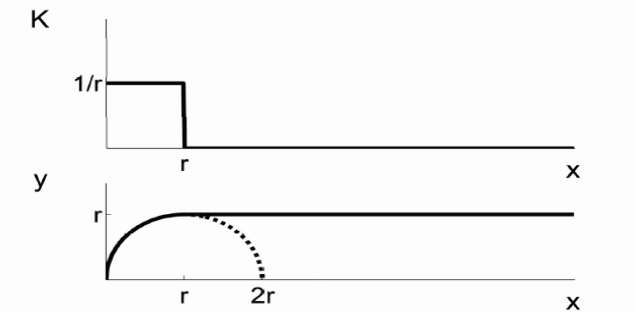

Figure 2.3: Curvature of a flat plate with circular leading edge

An ellipse with semi-axes a and b (with a>b), on the other hand, has a high curvature at its sharp side, equal to that of a circle with radius b^2/a, and a low curvature at its blunt side, corresponding to a circle with radius a^2/b. The curvature of an elliptic leading edge (a laying on the camber line) is therefore initially high a/b^2, but decreases rapidly and smoothly to its lowest value, b/a^2. The jump in curvature at the tangent

point is therefore much lower, as shown in next figure (same scale as Figure 2.4).The acceleration and especially the deceleration of the flow around an elliptic leading edge are milder than those observed with a circular leading edge. This keeps the spike in the cp profile low and helps to avoid the laminar separation.

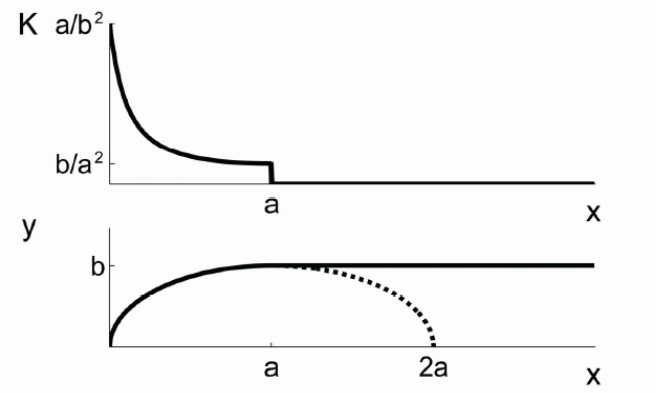

Figure 2.4: Curvature of a flat plate with elliptical leading edge

To conclude, a numerical example is given in next figure. On a flat plate, a circular leading edge with radius 1 is compared with an elliptic one having semi axes 1 and 3.

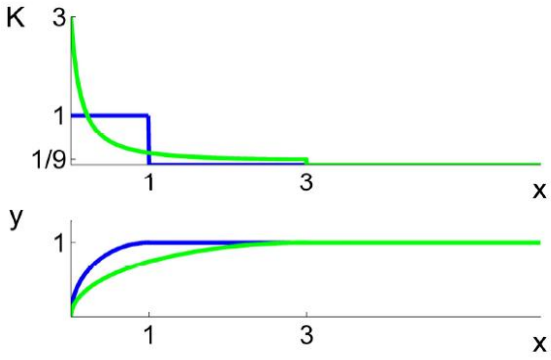

Figure 2.5: Circular vs elliptic leading edge

2.1.3 Effect of the Wedge Angle

The size of the C_p spike depends on curvature of the streamline and also on how long this curved path is. A flow particle is forced to follow a curved path from the stagnation point up to the wedge point. It is therefore clear that moving the wedge point

toward the stagnation point gives a shorter curved path and a lower spike. The only way to move the wedge point is to increase the wedge angle. In the example shown in following figure, a flat plate (0° wedge angle) and a profile with 90° wedge angle are compared. In the first case, the curved path is a quarter of the leading edge circumference, in the 90° wedge case; this is only one eighth of the circumference.

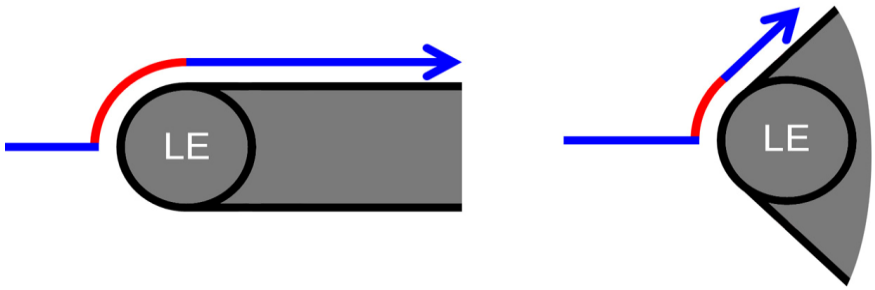

Figure 2.6: Streamlines around flat plate and 90° wedge

A high wedge angle is therefore helpful to keep the suction spike low and avoid the formation of a separation bubble.

2.2 LEADING EDGE LOSS

Tain L.et.al [1999] [14] Profile loss of a turbo machinery blade is a function of the momentum thickness at the trailing edge. The momentum thickness θ grows with the boundary layer along the whole profile and depends from the character of the boundary layer and from the initial value θ_0 at the leading edge. in a steady approach and in a similar way to what is presented by

$$\frac{\partial\theta(x)}{\partial x} + (H+2).\frac{\theta}{u(x)}.\frac{\partial u(x)}{\partial x} = \frac{C_f}{2} \quad \text{Eq. 2.3}$$

The skin friction becomes relatively small in the strong adverse pressure gradient. The right hand term is neglected and the equation can be rewritten.

$$\frac{\partial\theta(x)}{\partial x} < 0 \Rightarrow \frac{\partial P(x)}{\partial x} > 0 \Rightarrow \frac{C_f}{2} \approx 0 \quad \text{Eq. 2.4}$$

$$\frac{\partial\theta(x)}{\partial x} \approx -(H+2)\frac{\theta}{u(x)}.\frac{\partial u(x)}{\partial x} \quad \text{Eq. 2.5}$$

Some adjustments and integration lead to the following.

$$\int_0^x \frac{\partial\theta(x)}{\partial x} \approx \int_0^x -(H+2).\frac{\partial u(x)}{u(x)} \quad \text{Eq. 2.6}$$

$$\ln\left(\frac{\theta(x)}{\theta}\right) \approx -(H+2).\ln\left(\frac{u(x)}{u_0}\right) \quad \text{Eq. 2.7}$$

$$\theta(x) \approx \theta_0\left(\frac{u(x)}{u_0}\right)^{-(H+2)} \quad \text{Eq. 2.8}$$

The momentum thickness at the trailing edge is therefore proportional to that at the leading edge. This means that with a given lift distribution, a small variation in θ_0 is amplified and may lead to a large variation in the trailing edge momentum thickness and in the profile loss. A separation bubble is likely to be associated with an increase of θ. If the separation can be suppressed, a thinner boundary layer is expected over the whole chord, leading to lower loss values. As a final comment, an example to show the relevance of this analysis is given. To easily model an airfoil with separation bubble at the leading edge, it is common practice to trip the boundary layer directly at the leading edge assuming the whole flow to be turbulent. This is especially done in CFD, to avoid the problem of modeling the separation bubble. However, this method does not consider the effect of the bubble on the momentum thickness. θ_0 Is therefore wrong and the computed loss might be not reliable.

Martin N.Goodhand, et al. [2011] [5] Three different design of leading edges are investigated. it shows that the spike diffusion factor is kept below 0.1over the blades incidence range, performance is unaffected by leading edge geometry. The spike diffusion factor is given by

$$D_{spike} = \frac{u_{max}-u_{min}}{u_{max}} \quad \text{Eq. 2.9}$$

2.3 EFFECT OF WAKES

2.3.1 Effect on Incidence

The incoming flow has a given inlet angle, according to the velocity triangles. When wakes are present, the slip velocity of the wake relative to the free stream changes the inlet velocity triangle, as shown in next figure. This gives a positive incidence on the leading edge, since $\alpha_{1w} > \alpha_1$.

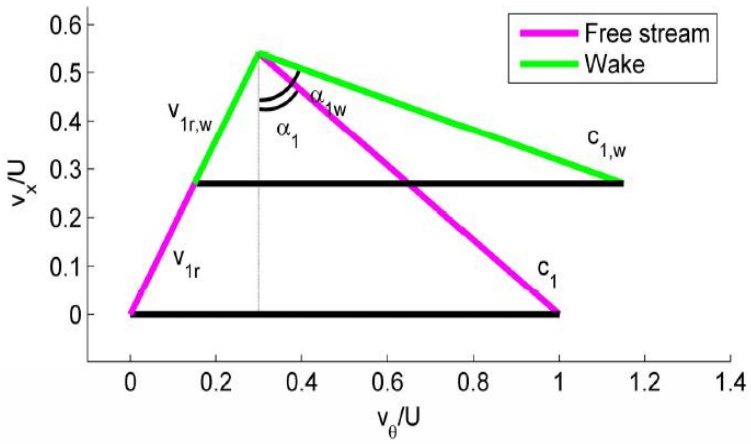

Figure 2.7: Stator inlet velocity triangle, with and without wakes

Wheeler A.P, et al. [2007] [15] For the same reason, the stagnation point migrates and the local incidence of the stagnation streamline in proximity of the leading edge also varies. it has been computed that the local incidence of the stagnation streamline is roughly 15° higher at the wake passage.

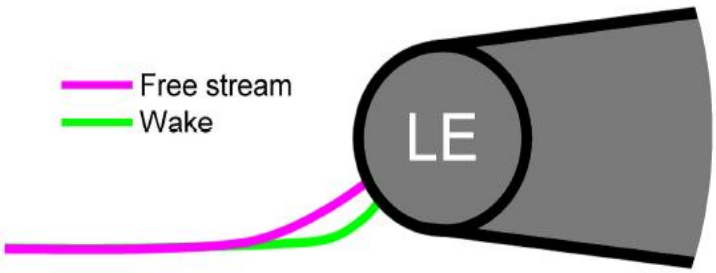

Figure 2.8: Stagnation streamline and local incidence

Because of this higher incidence, the flow needs to travel for a longer path around the highly curved leading edge. For this reason, the suction spike in the C_p gets probably higher when the wake passes and the boundary layer properties may vary. It is believed that the transition point on the suction surface migrates toward the leading edge, making a bigger part of the suction side turbulent. On the other hand, where a separation bubble is present, this would probably vary in size, growing when the wake passes. A pulsing behavior of the separation bubble could be expected. Following a quasi steady approach, according to Eq. 2.2-6, θ_0 and with it the momentum thickness at the trailing edge (and therefore the loss) should also pulse.

2.3.2 Wake Turbulence

Wheeler A.P et al. [2006] [16] The wake is also associated with a higher turbulence level. Show a free stream turbulence level of roughly 2.2% and a value in the wake of 4.5%.

This provides a tool to identify the wakes using unsteady measurement data: the wake should appear as a region of higher turbulence.

2.3.3 Wake-Boundary Layer Interaction

Wheeler A.P et al. [2006] [17] The interaction between the wake and the boundary layer has been studied using particle image velocimetry (PIV) and hot film techniques on the baseline blade. A vertical structure has been measured in the boundary layer. This is induced by the wake and is in phase with it at the leading edge. Then the structure convicts on the suction side with a convection velocity that is lower than that of the wake (between 60% and 70% of the wake velocity) and appears delayed at the trailing edge. The momentum thickness measured at the trailing edge shows a peak in phase with this structure, while no appreciable variation could be observed in phase with the wake. It is therefore this wake induced structure, and not the wake itself, to cause perturbations in the boundary layer.

Next figure is a contour plot of normalized vorticity and a vector plot of velocity perturbation. It shows the wake induced structure (marked with P) as a peak of negative vorticity. The wake (marked with W) and its relative slip velocity is also clearly visible.

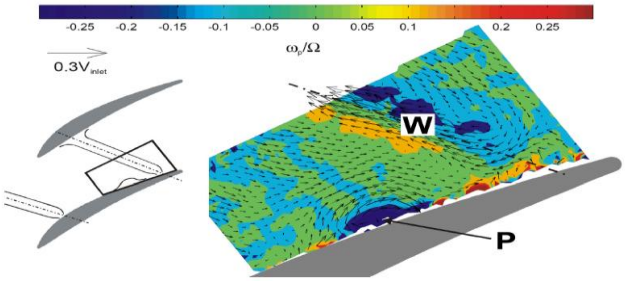

Figure 2.9: Velocity perturbation and contours of normalized vorticity

2.4 OTHER RESEARCH WORK ON AXIAL COMPRESSOR BLADE CASCADE

Wilcox, D.J.[1993] [18], the Reynolds-Averaged equations are

$$\frac{\partial U_i}{\partial x_i} = 0 \ldots\ldots\ldots\ldots\ldots\ldots\ldots\ldots\ldots\ldots\ldots\ldots\ldots\ldots Eq - 2.10$$

$$\rho\frac{\partial U_i}{\partial t} + \rho\frac{\partial}{\partial x_j}\left(U_i U_j + u'_j u'_j\right) = -\frac{\partial P}{\partial x_i} + \frac{\partial\left(2\mu S_{ji}\right)}{\partial x_j} \ldots\ldots Eq - 2.11$$

where μ is the dynamic viscosity, U is the mean velocity component, u' is the fluctuating velocity component which is related to instantaneous velocity (u_i) as

$$u_i = U_i + u'_i \ldots\ldots\ldots\ldots\ldots\ldots\ldots\ldots\ldots\ldots\ldots\ldots\ldots Eq - 2.12$$

s_{ij} is the strain rate tensor and is given by equation (2.12)

Aside from replacement of instantaneous variables by mean values, the only difference between the time averaged and instantaneous equations (equations 2.12 and 2.14), except the body forces, is the appearance of the correlation$u'_i u'_j$. This is a time-averaged rate of momentum transfer due to the turbulence. Herein lays the fundamental problem of turbulence [5]. $u'_i u'_j$Here, the concept of specific Reynolds stress tensor is introduced as follows

$$\tau_{ij} = -u'_i u'_j \ldots\ldots\ldots\ldots\ldots\ldots\ldots\ldots\ldots\ldots\ldots\ldots Eq - 2.13$$

τ_{ij} is a symmetric tensor, thus has six independent components. Hence, six unknown quantities are produced as a result of Reynolds averaging. Along with pressure and where

$$\varepsilon_{ij} = 2v\frac{\partial u'_i}{\partial x_k}\frac{\partial u'_j}{\partial x_k} \ldots\ldots\ldots\ldots\ldots\ldots\ldots\ldots Eq - 2.14$$

$$\rho C_{ijk} = \rho u_i^{\prime u_j \prime u_k \prime} + p' u_i^{\prime \delta_{ik}} + p^{\prime u_i \prime \delta_{ik}} \ldots\ldots\ldots\ldots\ldots\ldots\ldots Eq - 2.15$$

note that p' is the fluctuating component of pressure. this procedure also procedure also produces new unknowns like $u_i' u_j' u_k'$ $\left(\frac{\partial u'_i}{\partial x_k}\frac{\partial u'_j}{\partial x_k}\right)$, Illustrating the closure problem of turbulence. Because of the non-linearity of N-S equation, as higher and higher moments are taken, new unknowns are generated at each level. There is no way that the number of unknowns and equations can be balanced. The function of turbulence modeling is to establish proper approximations for the unknown correlations in terms of known flown properties so that a sufficient number of equations exists, in other words, to close the system of equations.

Chen, C.J, and Jaw, S.Y. [1998][19] summarized that from an engineering point of view, what an engineer would like to know is the mean effect of turbulence quantities and not so much the instantaneous fluctuation quantities. Thus, a more practical engineering approach to describe turbulent flow is to model the averaged turbulence quantities. When taking the ensemble average of the instantaneous Navier-Stokes equations, additional terms known as the Reynolds stress $U_i U_j$appear in the averaged Navier-Stokes equations, which makes the number of unknowns larger than the available equations. To close the problem, the Reynolds stresses have to be modeled, and additional differential equations related to turbulence characteristics may have to be introduced.

Ahmed et.al [1998] [20] studied the numerical simulation of steady flow in a linear cascade of NACA 0012 airfoils with control volume approach. The flow field is determined by two-dimensional incompressible Navier Stokes equations and the effects of turbulence are accounted by standard k- ε model. They investigated the boundary

layer developed at the suction and pressure surfaces of the airfoil, the pressure, lift and drag coefficients employing different angles of attack ranging from 0 to 24 degrees and solidities ranging from 0.55 to 0.83. They considered the incoming flow to the infinite linear cascade as turbulence free. At the inlet boundary, incoming flow velocity is specified and at the pressure boundaries, the pressure is specified. The inlet and outlet boundaries are extended to four and five times the chord length of the airfoil, respectively, to have a proper description of the flow. The periodic boundary condition is applied to simulate infinite cascade model. After an iterative solution procedure of the governing equations, they found out that the lift and drag force increase as the angle of attack increases, but the maximum obtainable lift is reduced as solidity increases because the upper surfaces of the airfoils are influenced by the pressure suppression of the neighboring airfoils. The slight decrease in drag force is observed as the solidity is increased and it is concluded that this is due to the movement of separation point to trailing edge because of the pressure suppression of the airfoils.

Widmann, J.F., et.al [2000][33] examined the flow through a vane –cascade swirl generator both experimentally and numerically. In the numerical analysis FLUENT is used. Two turbulence models, namely standard k-ε and RNG k-ε are employed for the turbulence models. The numerical simulations were generated using a segregated, implicit solver. The pressure and velocity were coupled using the PISO algorithm with neighbor and skewness correction, and standard wall functions were used for the near-wall treatment. When the RNG *k-ε* turbulence model was implemented, *the swirl-dominated flow* option was used. This option sets the swirl constant to 0.07.The authors meshed the computational domain with unstructured grid and modeled only 30o portion of it because of rotationally periodic symmetry in the swirl generator. The simulation results for the velocity magnitude at the outlet of the annulus using RNG k-ε model compared well with the experimental data, while the standard k-ε method fails to predict the recalculation zone observed near the inner wall of the annulus. The authors also computed the swirl number, which is an important parameter for the design of swirl generators, noting that this value should be validated with experimental results.

Lin, S.C. and Huang, C.L. [2002] [32] performed the analysis of a forward curved centrifugal fan both experimentally and numerically. The numerical simulation of the fan is done by a commercial CFD Code. The solution domain is divided into three parts, inlet region, rotor region and outlet region. These three parts have different mesh densities, according to the severity of the flow conditions. The results for CFD simulation served as a tool for arranging the diffuser section for low noise levels and adjusting the blade angles. The differences between experimental and numerical results were less than 5.4% for all the cases considered in the study.

Thole, K.A., Christophel, J.R., and Cunha, F.J.[2004][27] studied the cooling at the tip of a turbine blade cascade using pressure side holes. Both experimental and CFD analysis are performed to have optimum configuration of the pressure side holes. The experiments are done on a large scale, low speed, closed loop wind tunnel providing an inlet velocity to the test section. The test results are compared with a CFD analysis performed on FLUENT 6.0, which is a commercial software. The authors employed unstructured grid using GAMBIT, and solved the Navier Stokes equations along with energy equation. The RNG k-ε turbulence model is applied in the solution. The computations were performed on a single turbine blade exposed to periodic conditions along all boundaries in the pitch direction. The inlet boundary conditions were set as uniform inlet velocity at approximately one chord upstream of the blade. Inlet mass flow boundary conditions are imposed on the cooling holes. After the experimental and computational analysis, optimum configuration and sizes of the pressure holes are investigated.

Oh, K.J. and Kang, S.H. [2007][6] studied the dual performance characteristics of a small propeller fan. What is meant by dual characteristics is that the fan possesses radial type characteristics at low flow rates and axial type characteristics at high flow rates. They aimed investigating the sharp variation in the performance characteristics at low flow rates. Finite volume method is used to solve the continuity and Navier- Stokes equations in the flow domain around the fan. The configuration of the fan was such that the fan was operating at the inlet of an open circular chamber. The governing equations were the continuity and the Reynolds-averaged N-S equations for an incompressible,

viscous and turbulent flow. The Reynolds stresses are modeled using a modified k-ε turbulence model for swirling flows to account for a tangential velocity component imparted to the flow by the rotating fan. The employed boundary conditions were as follows:

1) Inlet and outlet sections: The stream wise gradient of flow variables is set to zero. The stream wise velocity component is corrected at the inlet and outlet planes so that the flow rate has a constant value.

2) Blade, hub and wall surface: The wall function method is employed. The first grid points next to the wall are placed in the logarithmic-law region and correlations of the wall function are imposed.

3) Periodic surfaces: Periodic boundary conditions are given on the periodic surfaces.

4) Wake centerline: Wake centerline conditions are given on the wake centerline. Several conclusions were drawn from the performed analyses. When circumferentially averaged flow velocities are used to find the flow pattern in axial and radial flow directions, it is observed that at low flow rates, the radial velocity is much larger than the axial velocity in the fan region and the fluid in the fan region moves along the radial streamlines. The flow showed an inflow toward the hub, and a radial outflow at the tip, which makes an angular momentum change in the flow between the inlet and outlet of the fan. This is likely to cause a rapid increase in static pressure rise and fan power. At high flow rates, the flow follows axial streamlines in the fan region as can be expected in a normally operating fan.

S. Fischer, H.S. et al. [2008] [21] With the aim to reduce the blade count in a stator row, in this paper the application of active blowing is discussed. Based on a high-speed compressor stage blade geometries for a stator cascade with jet flap implementation are developed. Two-dimensional numerical simulations of the cascade flow clarify that a reasonable appliance of the jet is particularly possible at high inlet flow angles, where the invested momentum can delay separation effects. At the compressor reference pitch the entrainment effect due to the jet energy broadens the

operation range. The blowing leads to a pronounced increase of the static pressure rise of about 9% in the design point. A stepwise increase of the pitch up to 20%, which is equivalent to a blade count reduction of about 16% in the present case, is considered. The worsen flow guidance through the cascade causes a reduction of the operation range, which is regained by the jet flap. The required mass flow of the jet, chosen in pre-studies, is about 1% which is an adequate amount for practical use in an engine.

P.K.Zachos et al. [2011] [22] performance prediction of axial flow compressors and turbines still relies on the stationary testing of blade cascades. In this paper, the performance of a 3-dimensional linear compressor cascade at highly negative incidence angle and objective of the research is to derive the total pressure loss and outlet flow angle through the blades and use the data for the validation-calibration of a numerical solver enhancing its capability to separated flows. The CFD model and the simulation presented.

Martin N.Goodhand, [2011] [23] Laminar boundary layers have lower skin friction than an equivalent turbulent layer. This property has long been exploited in the pursuit of low drag aerofoil sections for use on aircraft wings, but has not, until now, been used on the compressor aerofoil in jet engines In this paper a method, developed in collaboration with Rolls Royce during my PhD, which can achieve this is described. By carefully controlling the aerofoil's leading edge geometry it was found that significant extents of laminar flow could be maintained over the aerofoil's suction surfaces. These new, laminar flow compressor blades have recently been used to reduce the fuel consumption of the *Airbus A330.*

A. A. Adeniyi et al. [2012][24] They present a Large Eddy Simulation and k-ω SST turbulence model study for wakes in the flow field of a linear cascade of compressor blades using ANSYS-CFX. The gap in the endwall and the blade tip results pressure difference in the fluid flow thus generating wakes. it is discovered that the tip leakage vortex and the blade wake are characterised by a high velocity deficit. Blade-to-blade plot of stream wise vorticity below showed a wide range of flow structures

discussed in literature like the tip leakage vortex, separation vortices and trailing edge vortex shedding.

R.Azima et al.[2014][25] This paper written on the delay of boundary layer separation of 2D NACA 4412 by suction using CFD analysis. Transition flow over airfoils at the higher angle of attack shows lot of unsteadiness in flow such as local separation regions, boundary layer transition, turbulence. These phenomena are contains high energy loss and affects the aerodynamic loads in the form of lift loss and drag increase. by Controlling the flow through separation delay by suction at different slots, by flaps, by introducing bumps and sophisticated high lifting devices can mitigate the aerodynamic losses Picking out the right suction position augments the aerodynamic performance the selection of a suction position and outcome of different suction pressures at a definite slot. By suing suction at suction pressure 65kPa on 68% of the chord length of the airfoil with a constant angle 20 with the upper surface of the airfoil, AOA=13˚and M=0.6 the transition to turbulent flow about 91% of the chord length of the airfoil near the trailing edge. it is found at 43% of the chord length of the airfoil without suction. Along with this, at low angle of attack, the lift to drag ratio after suction increases about 2.24 times compared to that of without suction.

Zhang Haideng et al.[2015][26] With the aim of deepening the understanding of high-speed compressor cascade flow, this paper reports an experimental study on NACA-65 K48 compressor cascade with high subsonic inlet flow. With the increase of passage pressurizing ability, endwall boundary layer behavior is deteriorated, and the transition zone is extended from suction surface to the endwall as the adverse pressure gradient increases. Cross flow from endwall to midspan, mixing of corner boundary layer and the main stream, and reversal flow on the suction surface are caused by corner separation vortex structures. Passage vortex is the main corner separation vortex. During its movement downstream, the size grows bigger while the rotating direction changes, forming a limiting circle. With higher incidence, corner separation is further deteriorated, leading to higher flow loss. Compared with low aspect-ratio model, corner separation of high aspect-ratio model moves away from the endwall and is more sufficiently developed downstream the cascade.

A. Peyvan et al.[2016] [27] In this study, The design and off-design performance of a single stage axial compressor are predicted through 1D and 3D modeling. In one dimensional model the mass, momentum and energy conservation equations and ideal gas equation of state are solved in mean line at three axial stations including rotor inlet, rotor outlet and stator outlet. The total to total efficiency and pressure ratio are forecasted using the compressor geometry, inlet stagnation temperature and stagnation pressure, the mass flow rate and the rotational speed of the rotor, and the available empirical correlation predicting the losses. The 3D modeling is accomplished with CFD method. By defining the three dimensional geometry of the compressor and the boundary conditions coinciding with one dimensional model for the numerical solver, axial compressor behavior is predicted for various mass flow rates in different rotational speeds. Moreover, by comparing the results of one-dimensional and three-dimensional models with experimental results, The maximum differences of pressure ratio and isentropic efficiency of one dimensional modeling with experimental results are 2.1 and 3.4 percent, respectively.

T.Bain et al.[2016][28] it is investigated The effect of surface roughness on the boundary development and loss behavior of turbine blades with different Reynolds numbers. The result shows that the velocity profile in boundary layer is plumper on rougher face than on smooth blade. The aerodynamic loss is lowered at low Reynolds number at large at high Reynolds number. The total pressure loss coefficient of cascade can reach a top increase of 129% for rougher blades comparing with smooth blades at Re = 300000.

HongxinZhang et al. [2017][29] Unsteady pulsed suction (UPS) as a novel unsteady flow control (UFC) technique is applied in a certain highly loaded compressor cascade for the control of flow separations. Some related aerodynamic parameters such as excitation frequency and time-averaged suction flow rate are studied in detail. UPS and steady constant suction (SCS) are investigated to analysis comparatively the control effects of flow separations with the same time-averaged suction flow rate. The results show that UPS can provide appreciable improvement of cascade performance in a wide range of excitation frequencies. Based on the optimum frequency, the total pressure loss

coefficients under the time-averaged suction flow rates *ms*=0.4%and *ms*=0.53%are reduced by 9.4% and 14.2%, respectively. The time-averaged suction flow rate plays a more crucial role than the excitation frequency.

Behshad Ghazanfari et al. [2017][30] In this work, the stagger and camber angle of each blade are first changed while the other geometrical parameters such as overall camber, total stagger angle, the axial overlap, percent pitch and chord ratio are fixed. Secondly, the overall camber angle of tandem blade is changed by increasing the difference between the stagger angle of the first and second blade while the type of two airfoils, axial overlap and percent pitch, overall chord length and overall stagger angle are fixed. The aerodynamic performances of the generated tandem-blade cascades are obtained using two-dimensional numerical solution of flow. For this, a viscous turbulent flow solver is used for solving the Navier-Stokes equations. In these simulations, inlet Mach number is fixed to 0.6

CHAPTER 3

METHODOLOGY

3.1 BLADE DESIGN PROCESS

3.2.1 Preliminary Study

The wedge angle and the shape of the leading edge have been chosen as design parameters. A series of profiles with different wedge angles and with both circular and elliptic leading edge (3:1 axes ratio) have been designed and their loss coefficient Y_P has been computed with the two dimensional, steady CFD package (ANSYS)

Y_P is defined as the difference in the mixed averaged total pressure across the stage divided by the inlet dynamic head.

$$Y_P = \frac{P_{tot.out} - P_{tot.in}}{P_{tot,in} - P} \ldots\ldots\ldots\ldots\ldots\ldots\ldots\ldots\ldots\ldots\ldots\ldots\ldots\ldots\ldots\ldots\ldots\ldots\ldots\ldots\ldots\ldots\ldots\ldots\ldots\ldots\ldots\ldots\ldots .. Eq\ 3.1$$

Figure 3.1: Loss vs. wedge angle, Re=277,000, [4] This first analysis shows that for wedge angles bigger than roughly 30°, the elliptic and circular leading edge are more or less equivalent. On the other hand, for

smaller wedge angles, the elliptic leading edge proves to be much better than the circular one in keeping the loss low. This difference seemed to be associated with the presence of a separation bubble at the leading edge in case of a circular leading edge with low wedge angle. This separation bubble leads in general to worse boundary layer properties and to higher initial momentum thickness θ_0. Higher loss values are therefore expected. The process of separation and transition is strongly influenced by the Reynolds number. Previous figure shows the results of an analysis conducted at Re=277,000, that is the design Reynolds number. Real engine Reynolds numbers can be significantly higher, up to Re=1,800,000. Therefore, the same study has been repeated at higher Re, more representative of real engine conditions.

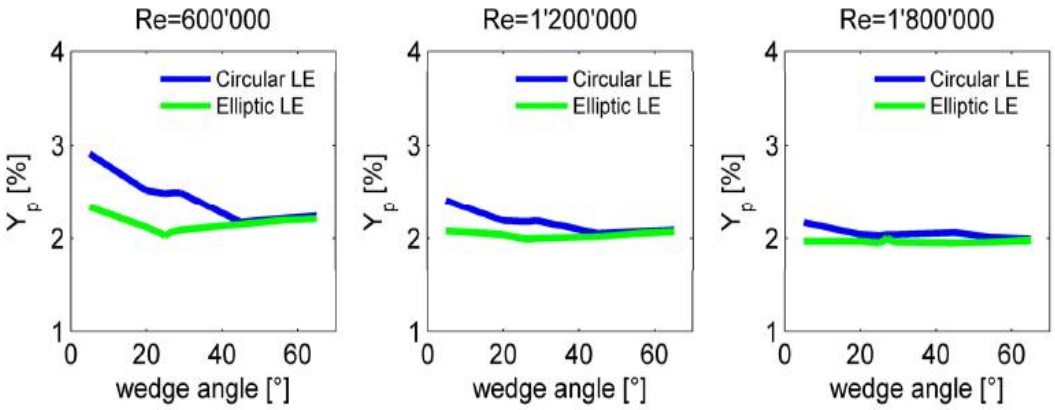

Figure 3.2: Loss vs. wedge angle, high Re [4].

As expected, the advantage of the elliptic leading edge at low wedge angle drops with increasing Re. This is because at high Re, transition occurs earlier and the separation bubble present on blades with circular leading edge and low wedge angle gets smaller or even disappears. However, even at high Re, the difference in Y_P is still relevant. The advantage of an elliptic leading edge is then significant also in real engine conditions.

The first task of the work was therefore to modify the baseline blade so that the new designed blades were more representative of real engine blades. This entails a smaller wedge angle and a reduced profile maximal thickness. The ratio between the leading edge dimension and the chord was also a fixed design constraint and has been

chosen to be similar to that of a real, high speed blade. The chord has been kept constant. Basing on these considerations and on the results presented in 3.1, the following three test cases have been chosen.

Blade A: 32° wedge angle, circular leading edge

Blade B: 15° wedge angle, circular leading edge

Blade C: 15° wedge angle, elliptic leading edge (3:1)

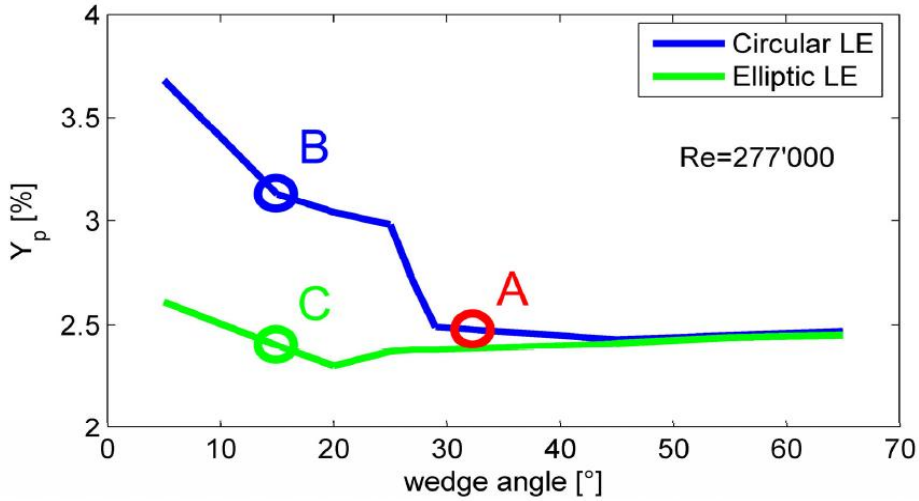

Figure 3.3: Test cases [4]

The blade A corresponds to the existing blades of the test rig. Blades B and C are the new designs. During the experiments, the blade set has not been entirely replaced. For the sake of simplicity and costs only one modified stator blade was used in the baseline set. To keep the aperiodicity as low as possible, the new blades could not be radically different; they should be as similar as possible to the baseline blades. Because the geometry has been changed only close to the leading edge, the aperiodicity is not expected to have large effects.

The final designed blades are therefore very similar to the baseline, except in the region close to the leading edge. The wedge angle has been roughly halved and the leading edge has been thickened. The maximal thickness is only slightly smaller than

that of the baseline blades. Finally, two leading edge shapes have been designed: circular and elliptical.

3.2 DESIGN PROCESS

3.2.1 Geometry Modification

A JAVAFOIL and CAD software has been used to modify the blade geometry. The routine reads the coordinates of each section from the blade definition file of the baseline blade, computes the camber line and the thickness distributions of both suction and pressure side, calls a subroutine to modify the thickness distributions at the leading edge and reconstructs the airfoil from the camber line and the new thickness distributions. Finally the new coordinates are written in a new blade definition file.

The thickness distribution is modified according to following procedure. First of all the new leading edge shape (a circle or an ellipse of given dimension) is imposed and the wedge point is set. Its position is univocally fixed by the chosen wedge angle; the wedge point is by definition the point where the leading edge is tangent to the line having the slope equal to the tangent of the wedge angle. Then, a cut point on the blade surface must be chosen and finally a curve must be fitted between the cut point and the wedge point. A Bezier curve has been chosen for this purpose.

An approximated design modification of blades are shown in the below diagram.

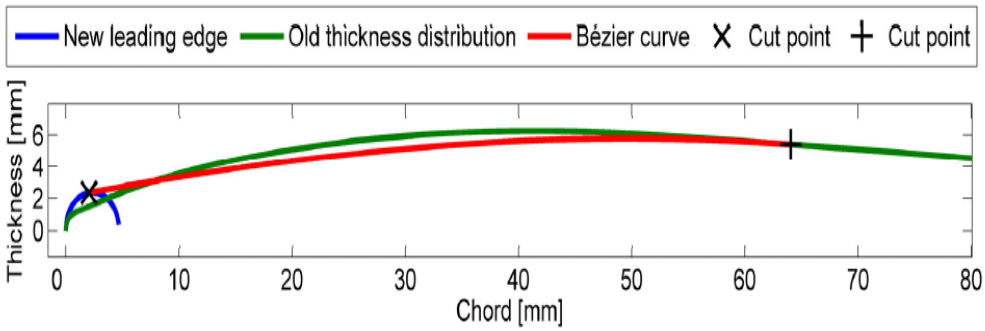

Figure 3.4: Modified thickness distribution [3]

3.2.2 Design Tool

The geometry of the new designed blades and the flow field around them should be as similar as possible to the baseline blade. To check the agreement between the different flow fields, javafoil has been run on each new designed profile and the new C_P distribution has been compared with the baseline. The design process was therefore a strongly iterative procedure, where efforts have been made to understand the effect of geometrical constraints like the position of the cut point and the properties of the Bezier curve.

Intuitively, since the airfoil is only modified from the leading edge to the cut point (where the curve is fitted), it can be supposed that the cut point should be set in proximity of the leading edge. However, since the size of the leading edge and the wedge angle are radically different, as a good compromise, the position of the cut points of the new blades varies spanwise between 50% and 60% of the chord.

3.3 BLADE A

The blade A is the baseline stator blade. Its design was not part of this work; the leading edge is circular with 2.3 mm diameter. The wedge angle is 32°. At mid-height, the inlet metal angle is 52.3° and 25.0° is the exit one, as given in next figure. The true chord is 126 mm and 74.4 mm is the axial chord.

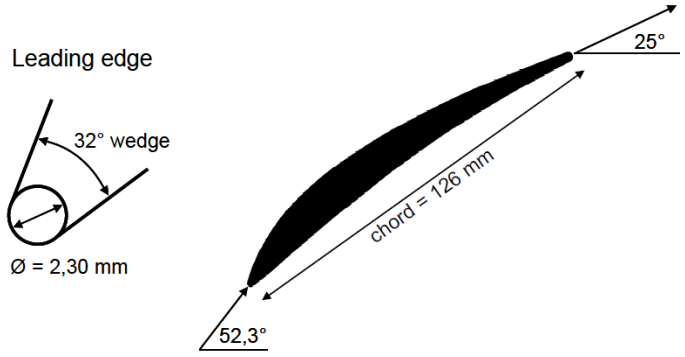

Figure 3.5: Baseline geometry BLADE A, mid-height [4]

Given the profiles of the pressure coefficient C_f, shape factor H and friction coefficient C_f shown in figure 3.7, 3.8 and 3.9. Javafoil has been run at the same conditions of the ANSYS. The inlet velocity and the mass flow have been set to match the design flow coefficient of the ANSYS of 0.51, the inlet flow angle is 52,3°

The computed loss coefficient Y_p is 2.38% .A suction spike at the leading edge is present. It is relatively small and the downward side does not present any kink. This suggests that the boundary layer stays laminar and does not separate.

The shape factor of the suction side is initially 2.5, and then has a peak at about 20% of the chord and drops subsequently to 1.7. The peak in H is the transition point. As the shape of the leading edge spike suggested, a laminar boundary layer up to 20% chord and a turbulent one afterwards. A kink is also present in the C_p profile at the same position. C_p does not reach zero at any point. This means that no separation is present. This is particularly important at the leading edge and is consistent with the remarks above: if a separation bubble at the leading edge was present, the boundary layer would have been turbulent from the beginning. The very high peaks in the C_f distribution at the leading edge correspond to the stagnation point, where the stagnation streamline impinges.

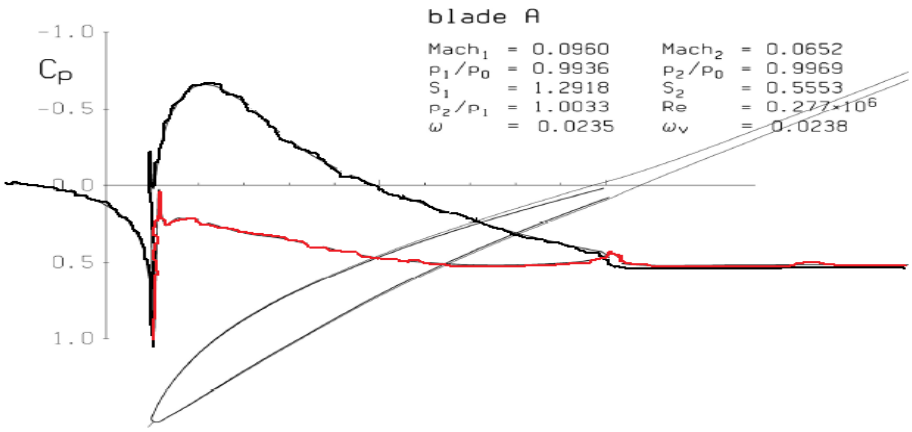

Figure 3.6: variation of coefficient of surface pressure vs relative chord ratio for BladeA.

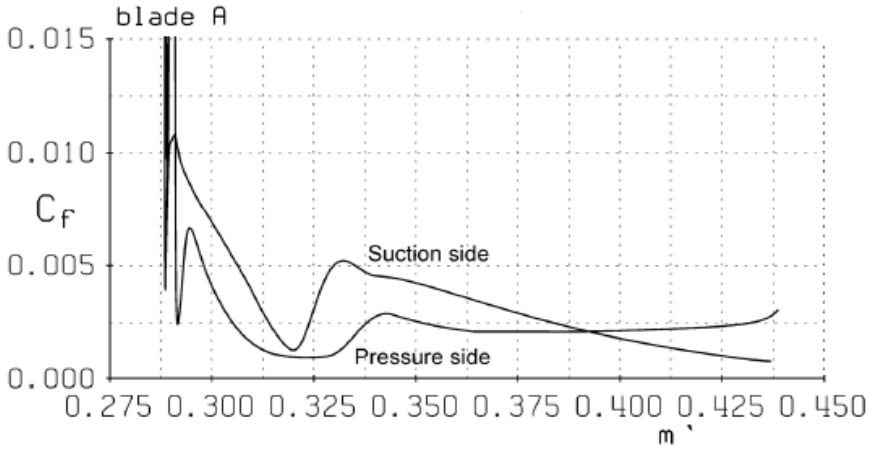

Figure 3.7: variation of skin friction coefficient vs. relative chord ratio for Blade A.

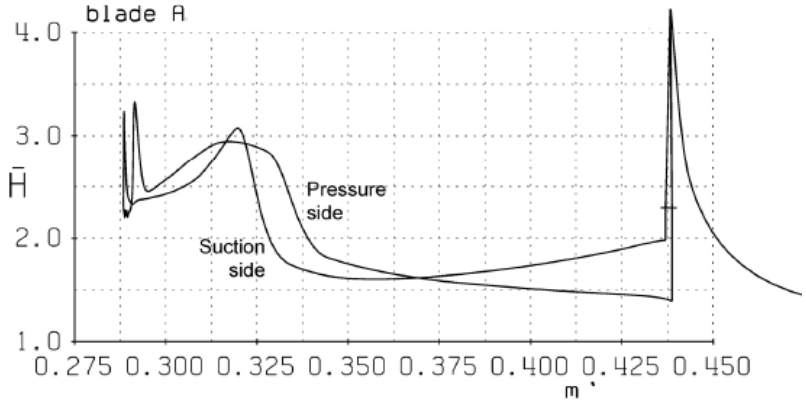

Figure 3.8: variation of shape factor vs. relative chord ratio for Blade A.

3.4 BLADE B

The blade B has a thick, circular leading edge. The leading edge diameter is 4.72 mm and the wedge angle is 15°.The camber line has not been modified and the metal angles are therefore the same. The geometry of the mid-height airfoil is shown in next figure.

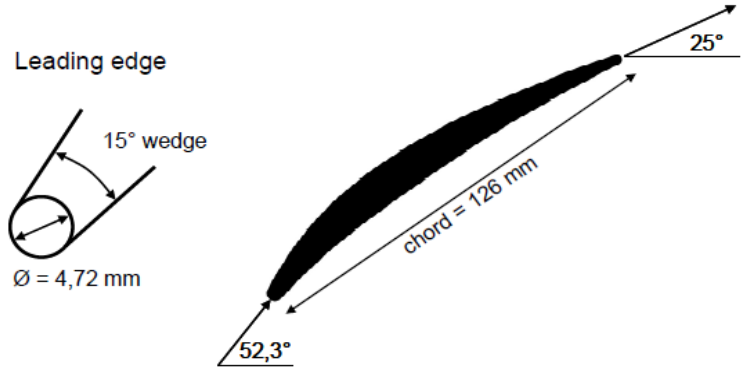

Figure 3.9: Geometry of blade B, mid-height [4].

Javafoil has been run on this blade at the same conditions and at mid-height, with the results shown in Figure 3.10, 3.11 and 3.12.

The biggest difference is the much higher leading edge spike at the leading edge on both surfaces, due to the different geometry. A kink on the downhill side of the spike is visible, revealing the presence of a separation bubble. The peak suction point is also slightly lower than on blade A.

The H profile shows a high and sharp peak near the leading edge, at the wedge point. It corresponds to the separation bubble. Afterwards, the reattached boundary layer is fully turbulent and the value drops immediately to 1.7.

The friction coefficient goes to zero near the leading edge, proving definitively the presence of a separation bubble.

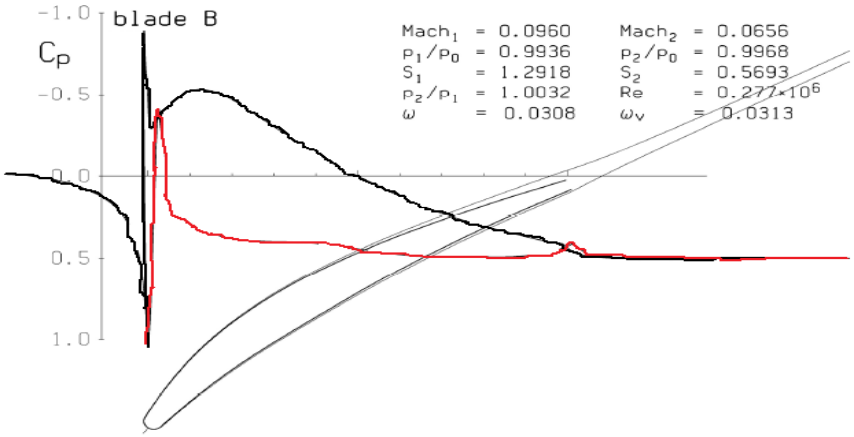

Figure 3.10: variation of coefficient of surface pressure vs relative chord ratio for BladeB.

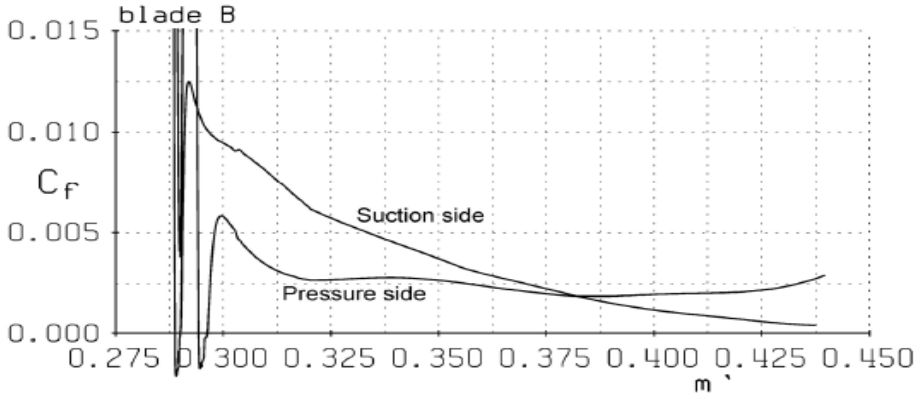

Figure 3.11: variation of skin friction coefficient vs relative chord ratio for BladeB.

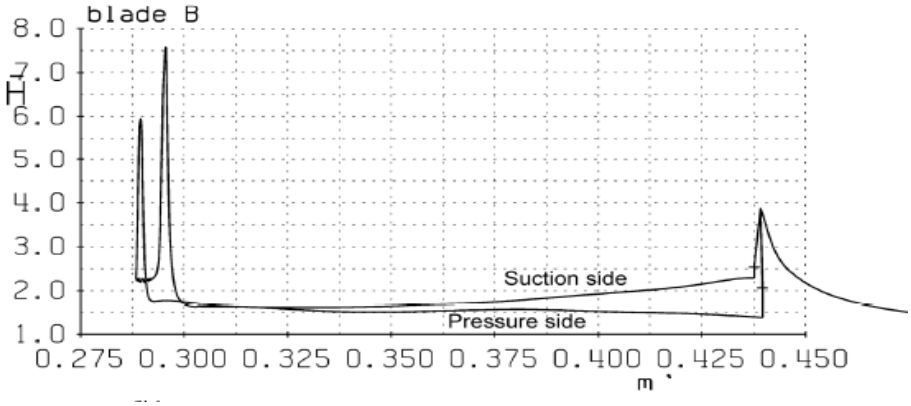

Figure 3.12: variation of skin friction coefficient vs relative chord ratio for BladeB.

3.5 BLADE C

The blade C is based on blade B; the blades are perfectly the same, except the shape of the leading edge, which is now elliptic with the axes ratio being 3:1. The wedge angle is again 15°.

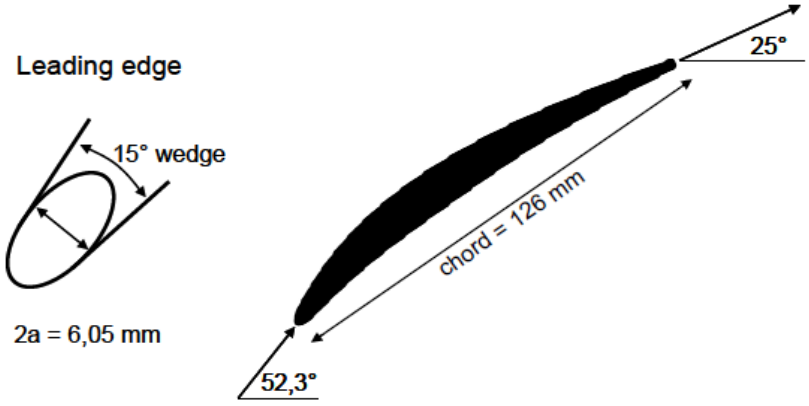

Figure 3.13: Geometry of blade C, mid-height [4]

On this geometry javafoil gives the results plotted in Figure 3.14,3.15 and 3.16. The suction side cp is very similar to blade B, except near the leading edge spike. The elliptic leading edge makes it almost disappear and part of the boundary layer can be assumed to be laminar. A kink can be observed again after the peak suction point, showing probably the transition point.

The H profile of the suction surface is similar to the profile computed for the baseline blade. A similar interpretation leads to the conclusion that the boundary layer is laminar for roughly 20% of the chord and turbulent afterward. On the other hand, the H spike on the pressure surface appears to be near the wedge point, suggesting the presence of a separation bubble on the pressure surface. However, the height of the spike (3.75) is relatively low, much lower than those found at the wedge points of blade B (6 on the suction side ant 7.5 on the pressure side). The friction coefficient at that point is also very low, but not zero. It is therefore difficult to predict if the flow really separates at the

wedge point on the pressure surface. In any case, the H value shows the turbulent character of the boundary layer downstream the wedge point.

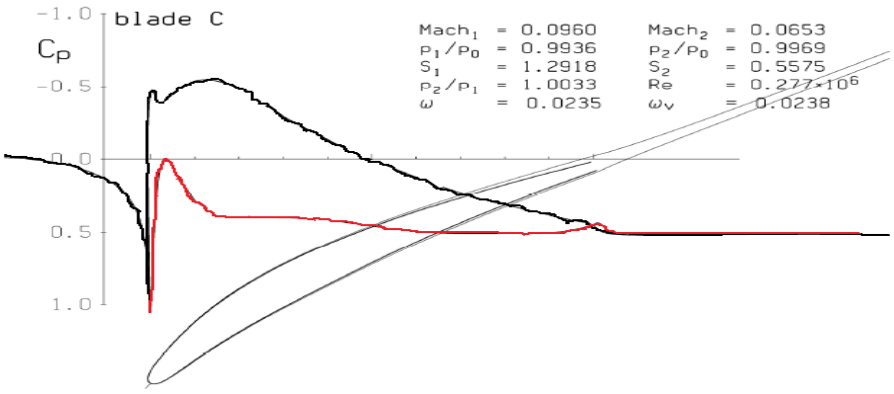

Figure 3.13: variation of coefficient of surface pressure vs. relative chord ratio for BladeC

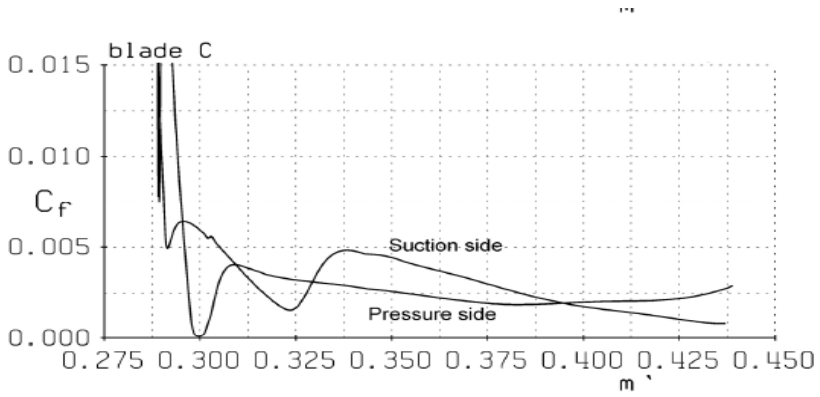

Figure 3.14: variation of skin friction coefficient vs. relative chord ratio for BladeC

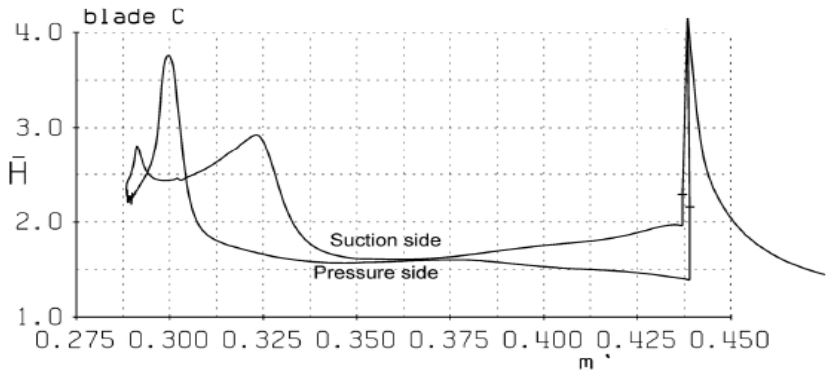

Figure 3.15: variation of shape factor vs. relative chord ratio for BladeC

3.6 COMPARISON

In next figures, the mid-height profiles of blades A and B are drawn together, and the C_p distributions are superimposed. This direct comparison shows the effect of the wedge angle variation. where the wedge angle is high, the path around the leading edge circle is shorter. The flow is less accelerated and the leading edge peak is lower.

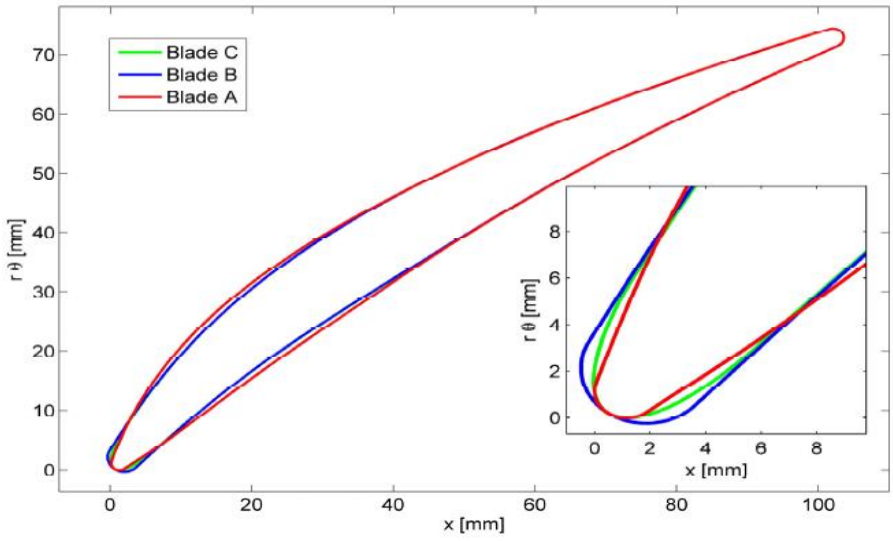

Figure 3.16: Mid-height blade profiles

The difference in the peak suction and generally in the whole C_p profile is likely to cause some aperiodicity, since only one blade has been replaced. The peak suction is lower because the modified blade is thinner and its curvature at the throat is lower. The designed profiles are the results of an iterative process which aimed to obtain a C_p distribution as similar as possible to the baseline one. However, it was not possible to build a blade with exactly the same C_p distribution (except at the leading edge) as the baseline one, with such deep modifications in the leading edge dimensions and in the wedge angle; especially considering that most of the geometrical constraints were more or less fixed. In any case, the results of this work are believed to be only slightly affected by the aperiodicity and no change in the conclusions is expected.

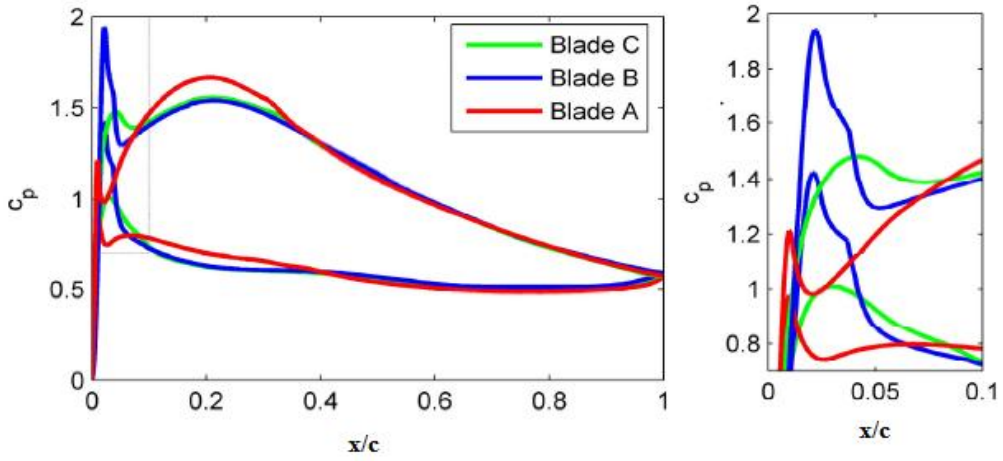

Figure 3.17: Computed cp distribution, all blades[4]

A direct comparison between blades B and C shows the effect of the different leading edge geometry on the suction spike. As expected, the cp distribution is the same but the suction spike with the elliptic leading edge is much lower and no separation is present.

3.7 ANSYS AS A MODELLING TOOL OF CASCADE BLADES

3.7.1 Model domain and boundary conditions

In the design phase of the axial flow compressor blade, it will be assumed that there is no radial component of the velocity at the blade inlet and the pressure rise across the rotor is constant in the radial direction (free vortex design). As a result, pressure difference does not occur across the streamlines at the exit of the rotor and the streamlines consist of only axial and tangential components. Due to this fact, the aerodynamic performance is computed on a two-dimensional plane. In an axial turbomachine, the blades can be thought as if they lie on a line of infinite length so the solutions are obtained for an infinitely long linear cascade of blades.

The blades are arranged in linearly with solidity$(\sigma) = 2$ where $\left(\sigma = \frac{s}{c}\right)$ and inlet flow angle may vary from 0˚ to 30 ˚ to verify the best flow visualization.

The computational mesh is generated with ANSYS (mesh module), which is the pre-processor of FLUENT 16. There are three types of profiles i.e. blade A, blade B and blade C are located in a flow passage domain through which the air stream passes. The mesh is composed of triangular elements. A sample of computational domain is given in Figure (3.18).

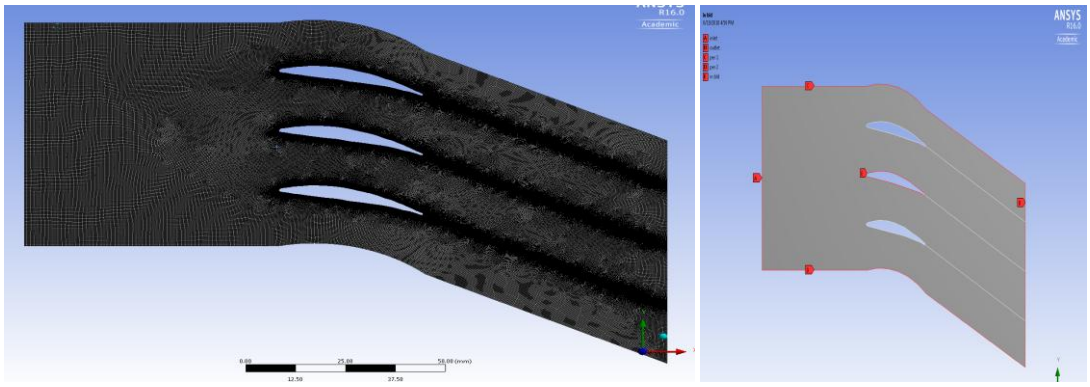

Figure 3.18 Meshing of blade cascade and boundary condition for zero degree incidence.

The 2D modeling scheme was adopted in ANSYS. The structured grids were generated using ANSYS meshing tool. It can be done in forms namely edge meshing, face meshing. Structured grid cells are used for entire domain. Cells are clustered at the region in face or 2D meshing the following parameters can be specified. Meshing schemes mesh node spacing and face meshing options. The meshing schemes include the elements and the types. The mesh is composed of triangular elements.

In order to obtain an O-grid around the airfoil, Inflation is to be utilized. Under Mesh Control Inflation is selected. Edge cube and specify the four edges of the airfoil. Specify 20 Layers with a Growth Rate of 1.1. Set the Maximum Thickness according to Y+ value calculation.

To estimate the first cell height, we begin by calculating the Reynold's number:

$$Re = \frac{\rho UL}{\mu} \ldots\ldots\ldots\ldots\ldots\ldots\ldots\ldots\ldots\ldots\ldots\ldots\ldots\ldots\ldots\ldots Eq - 3.2$$

but in case of aerofoil shaped object the Reynolds number is calculated by

$$\text{Re} = v * C * 70000 \ldots\ldots\ldots\ldots\ldots\ldots\ldots\ldots\ldots\ldots\ldots\ldots\ldots\ldots\ldots\ldots Eq - 3.3$$

Re= 277000 (Chord Reynolds Number, Incompressible Case)

The Y+ value is then given by

$$Y+ = \frac{\rho u_f \Delta s}{\mu} \ldots\ldots\ldots\ldots\ldots\ldots\ldots\ldots\ldots\ldots\ldots\ldots\ldots\ldots\ldots\ldots Eq - 3.4$$

as per standard results it is recommended that the Y+ value should be in between 1to11. for this calculation Y+ value is 10.225.

Table 1.0 Mesh details and boundary condition,

Sizing		Inflation	
Use Advanced Size Function On	Curvature	**Inflation Option**	First layer thickness
Relevance Center	Fine	**Transition Ratio**	0.272
Smoothing	High	**Maximum Layer**	12
Max Face Size	1.74 mm	**Growth Rate**	1.1
Max Size	2.333 mm	**Statistics**	-
Growth Rate	1.20	**Nodes** **Elements**	214039 212082

3.7.2 CFD Setup

The two dimensional meshed file have been imported in FLUENT software then it is created two periodic after that it has been analyzed in grid or mesh mode and finally it has been analyzed with pressure based, steady state, k- epsilon (2 equation) model is used to analyses the 2D cascade model. In solution method we gave 1000 iteration for each velocity. The iteration is converged after about 670 iteration the convergence criteria set 0.0007 which will give good result as per requirement. Convergence graph given in the figure below.

If inlet velocity increases the laminar boundary layer was small in fraction and turbulent boundary layer was about 60-70 % of the span length this transition of boundary layer over the span length is leading to wake at trailing edges. Reynolds number at inlet is main factor for developing wakes at trailing side.

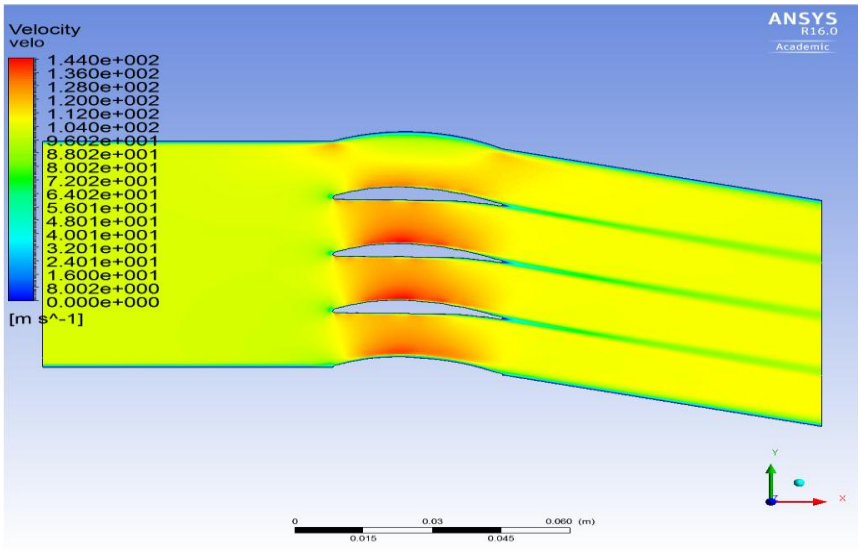

Figure 3.19 Velocity contour at 2D cascade blade shows wake at trailing edge.

Velocity contour shown in figure (3.17) the fluid flows over blade surface wake created near the trailing edge.

The 2D cascade can visualize only the flow over profile. It is not give any information about the fluid characteristic over the blade surfaces so to avoid these difficulties and to get more accurate knowledge for flow in the blade surface i.e. suction surface. We create a 3D cascade model.

The numerical simulations were implemented by means of the commercial software CFX to solve the steady Reynolds Aver-aged Navier–Stokes (RANS) equations. The *k*–ε̇ turbulence model as a suitable turbulence model has also been well applied in certain compressor cascades due to its highly accurate pre-diction ability in the presence of flow separation. Therefore a high-resolution scheme and a second-order backward scheme were used. At each time-step, the convergence criterion is that normalized RMS residuals are less than 7.0 $\times 10^{-5}$. The steady flow accelerates convergence. Data were recorded only if the total parameters laid in the wake as monitor probes converge to a periodic solution. An O-type structured grid was generated in TURBO GRID. Grid encryption was employed around the blade wall and the endwalls to ensure that the details of the boundary layer flow were captured exactly. The *y*+ of the

blade wall and the endwalls was less than 10, which could meet the demands of the turbulence model.

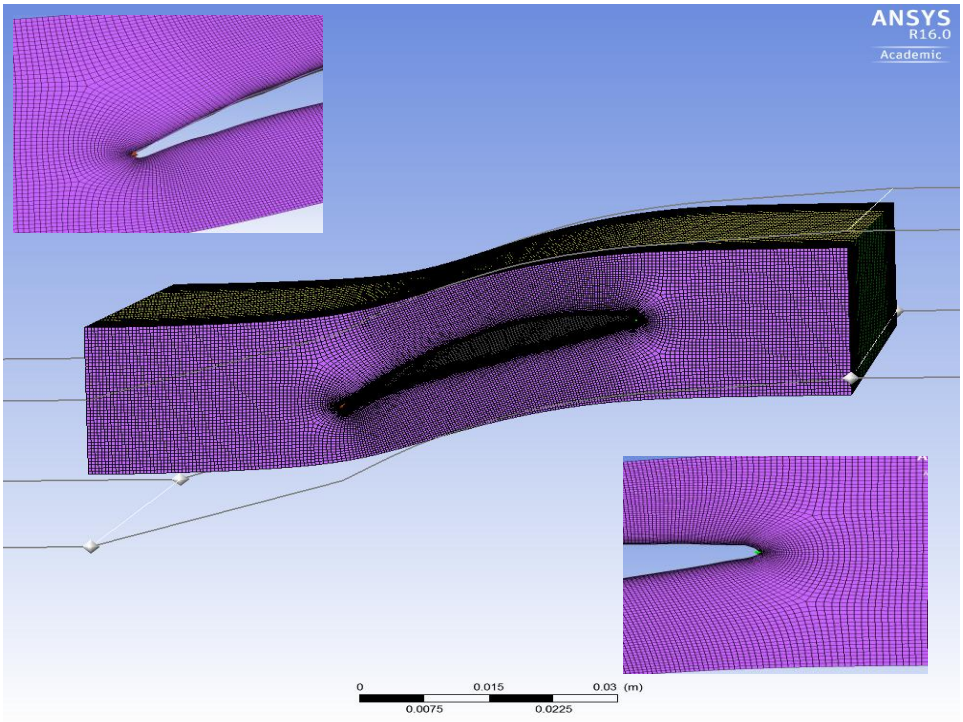

Figure 3.20 3D cascade mashing at leading and trailing edge

Table: 2 Mesh detail for 3D cascade model

Domain	Nodes	Elements
R1	1490670	1435570

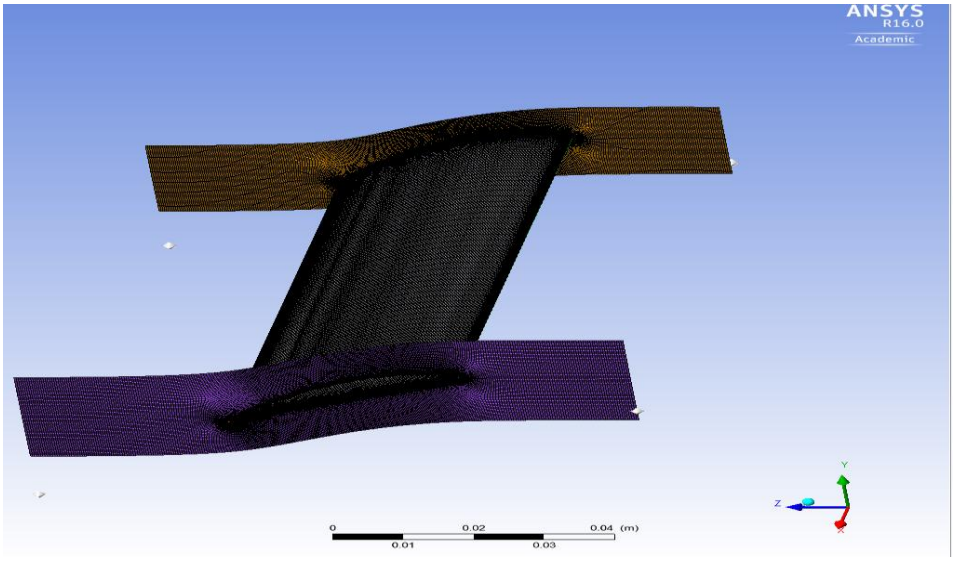

Figure 3.21 3D cascade meshing for blade surface

3.7.3 Flow Visualization

The flow inside an axial compressor is three dimensional but the measurements have been taken only at mid height, assuming a two dimensional behaviour. To investigate if this assumption was appropriate, some flow visualization was necessary, aiming to show any three dimensional feature of the flow around the test blades.

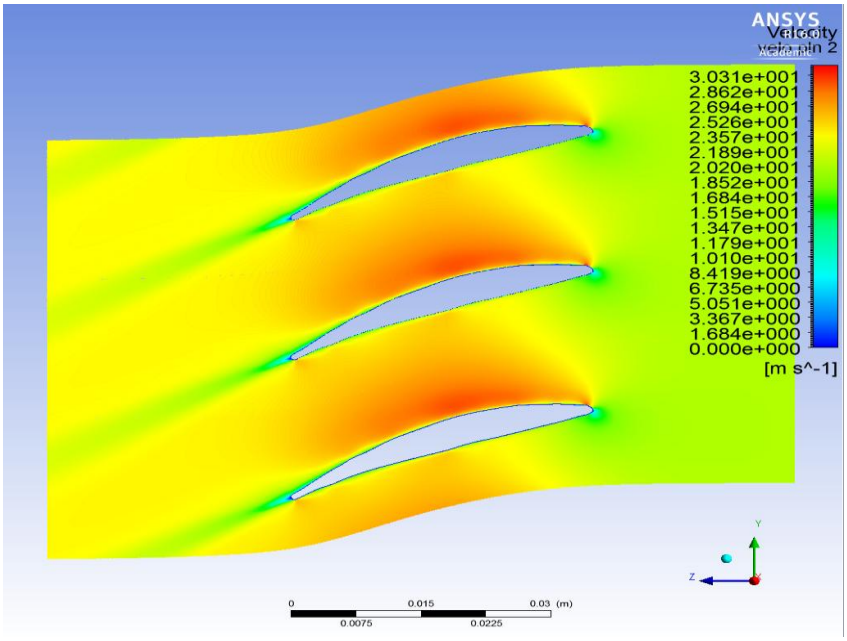

Fig.3.22 Velocity contour at mid plane

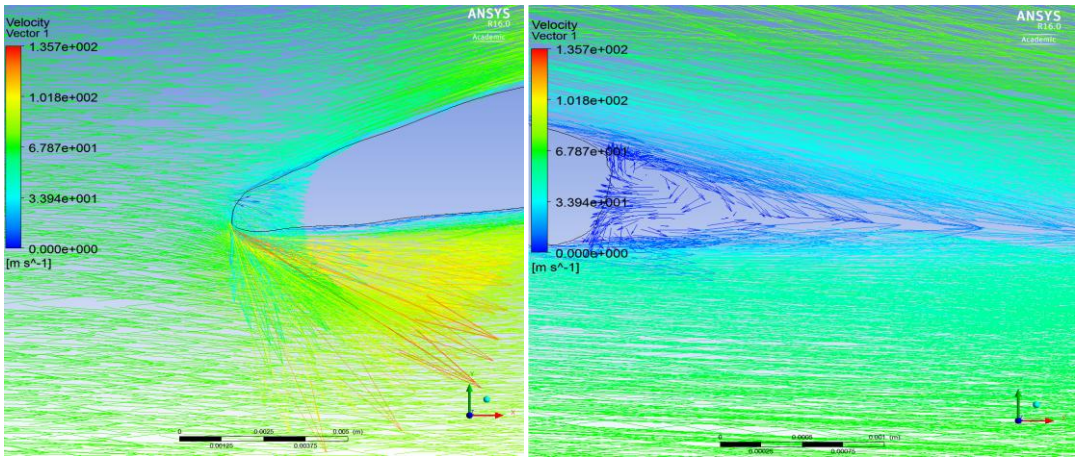

Figure 3.23 velocity vector at leading edge and trailing edge

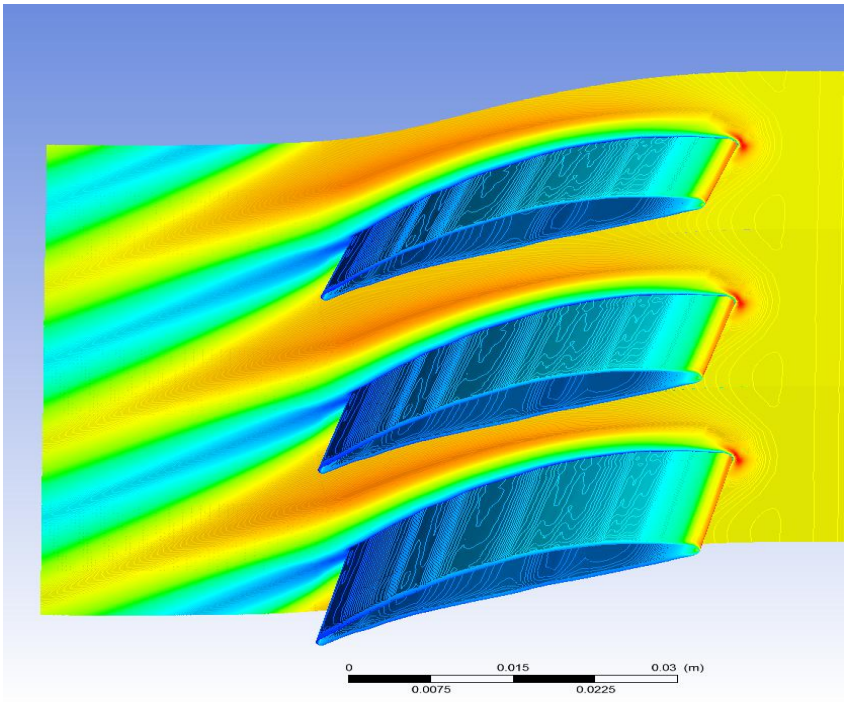

Figure 3.23 Contour of turbulence eddy at hub part and blade surface

Fluid interacts with leading and trailing edge .wake developed at the trailing side and interaction of fluid over leading edge boundary layer due curvature of the blade profile.

CHAPTER 4

SIMULATION AND RESULT VALIDATION

4.1 C_p MEASUREMENTS

The measured $C_p$profile for the three blades is here plotted against the non dimensional relative chord ratio X/C As a comparison; the profile computed by ANSYS (Fluent) is also shown. The spike at the leading edge (dashed rectangle, zoomed in the left plot) is finely resolved. Some difference in the peak suction point and generally in the suction surface profile is present this difference is more or less consistent for the three blades.

On the blade A, the spike is relatively narrow and sharp, as predicted by the CFD. It is slightly higher and wider than the computed one. No separation bubble could be observed, it is therefore difficult to assess where transition occurs. In any case, the results do not show it to happen at the leading edge, a certain fraction of the surface can be assumed to be laminar.

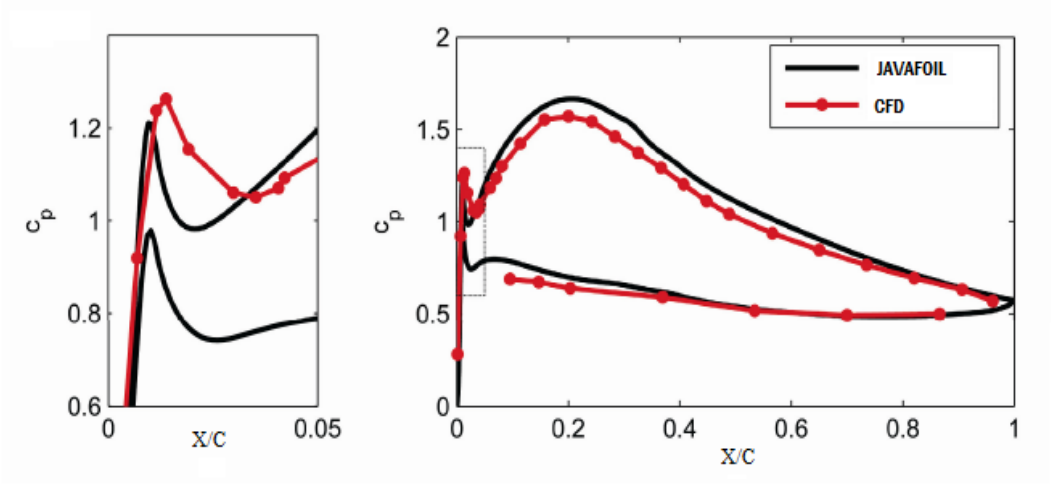

Figure 4.1: Measured C_p profile of blade A in ANSYS and JAVAFOIL prediction

A sharp and much higher spike is present on blade B. the flow separation on both surfaces could be investigated. It is shown by the small region of more or less constant static pressure on the surface.

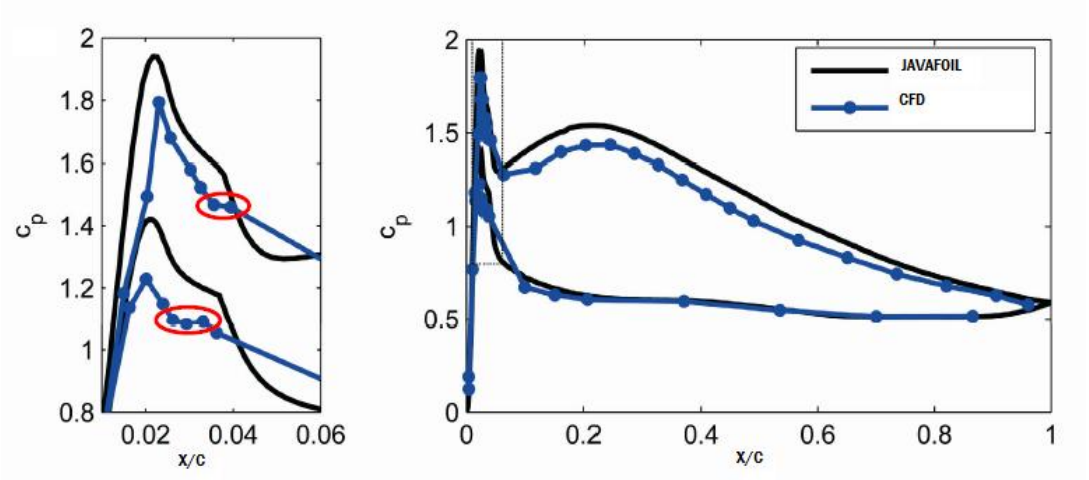

Figure 4.2: Measured C_p profile of blade B in ANSYS and JAVAFOIL prediction

The reattached boundary layer is turbulent. This leads to the conclusion that the boundary layer on the whole blade is turbulent, that is in agreement with JAVAFOIL prediction. The different geometry of blade C leads to a lower and less sharp spike. Similarly to blade A, no leading edge separation bubble on the suction side could be observed. Again, the boundary layer of part of the suction surface is likely to be laminar.

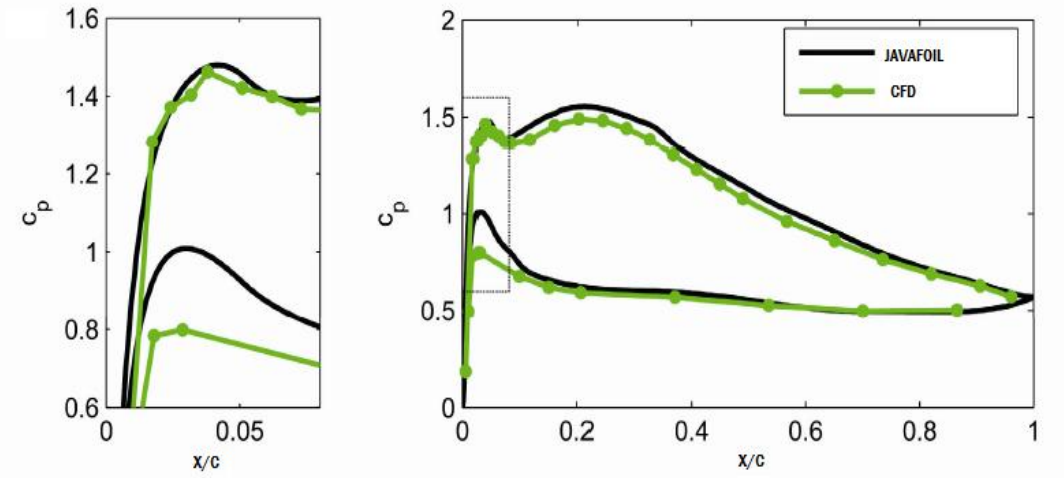

Figure 4.3: Measured C_p profile of blade C in ANSYS and JAVAFOIL prediction

The pressure surface spike is considerably lower than the computed one. Predicted a separation on the pressure surface this does not appear in simulation.

4.2 WAKES AND LOSS

A five blade cascade downstream we go for measure the three blades at middle and leave the outer blades due to end wall effect in the test section. The pitch wise total pressure profiles are showing the wakes. The width and depth of the wake give a measure of the loss coefficient Y_p, the wakes of the three test blades are plotted in next figure.

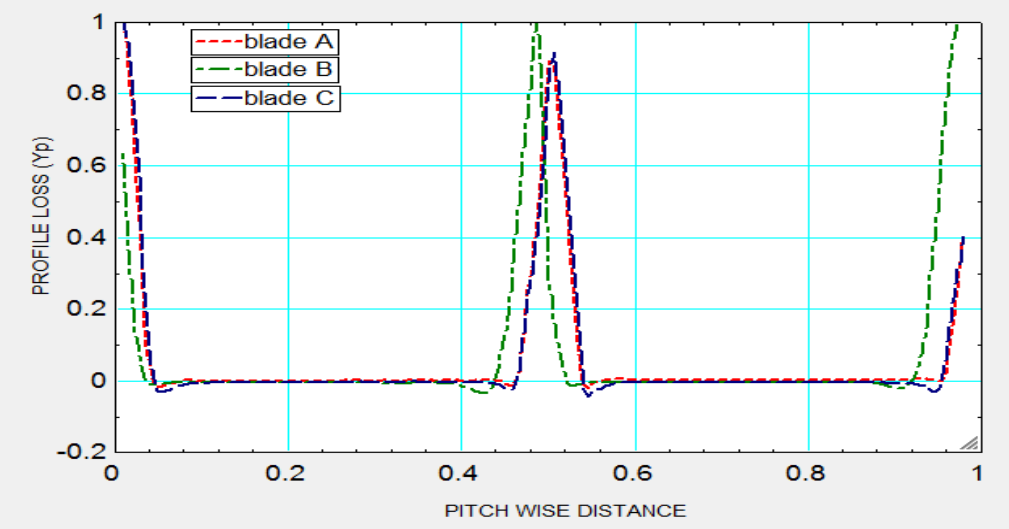

Figure 4.4 Profile losses of blade A blade B and blade C

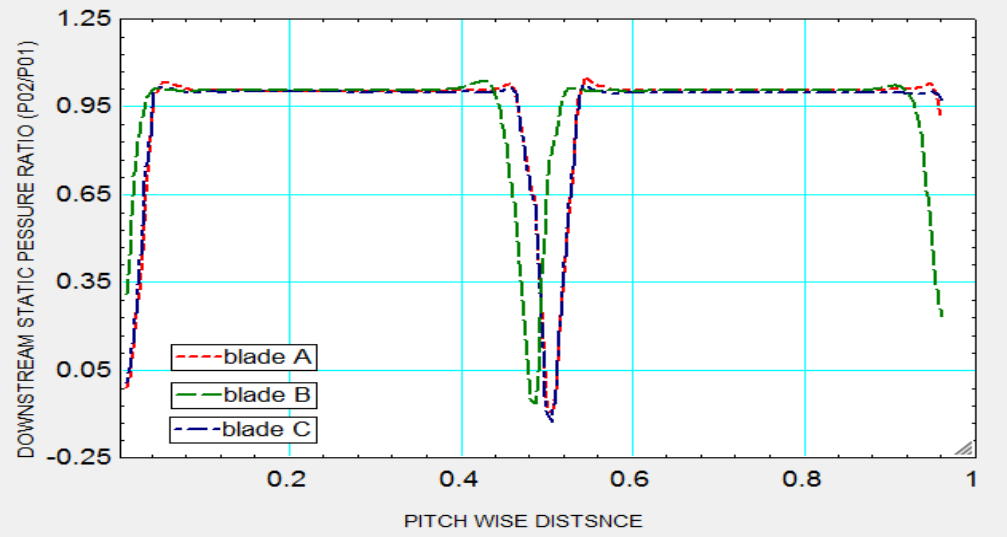

Figure 4.5 Downstream static pressure ratio of blade A blade B and blade C

After the calculation area loss averaged of the profile losses graph above figure

It found that the loss coefficients Y_p for the three blades are:

Blade A: Y_p=2.5%

Blade B: Y_p=3.3%

Blade C: Y_p=2.5%

Clearly, the highest loss value is associated with the widest and deepest wake: B. A and C have similar wake profiles and therefore similar loss.

The higher loss of blade B is due to the presence of the separation bubble. The reattached boundary layer is turbulent on the whole blade, leading to higher loss values. Moreover, across the bubble the momentum thickness grows significantly. This influence θ_{TE} and therefore the loss. The difference between JAVAFOIL and CFD is around 0.12% for blades A and C and roughly 0.17% for B. The wake B is also slightly shifted; it may be showing a small difference in exit flow angle.

4.3 BOUNDARY LAYER UNSTEADINESS

The upstream rotor blades produce their own wakes, which hit the leading edge of the test blades and interact with their boundary layer. This interaction leads to unsteady phenomena in the boundary layer, which must be investigated to gain some understanding on the effect that the wakes have on the loss. In this case, the FLUENT data have been used to give an interpretation of the transient behavior of the trailing edge momentum thickness.

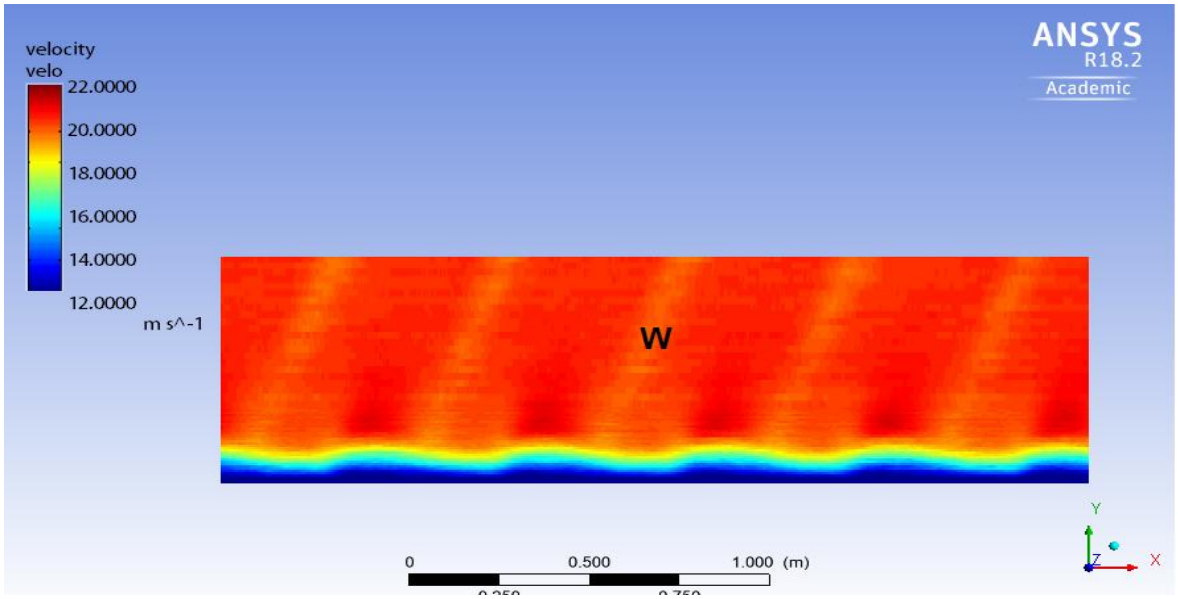

Figure 4.6 Velocity field for blade A, over suction surface, (ensemble average)

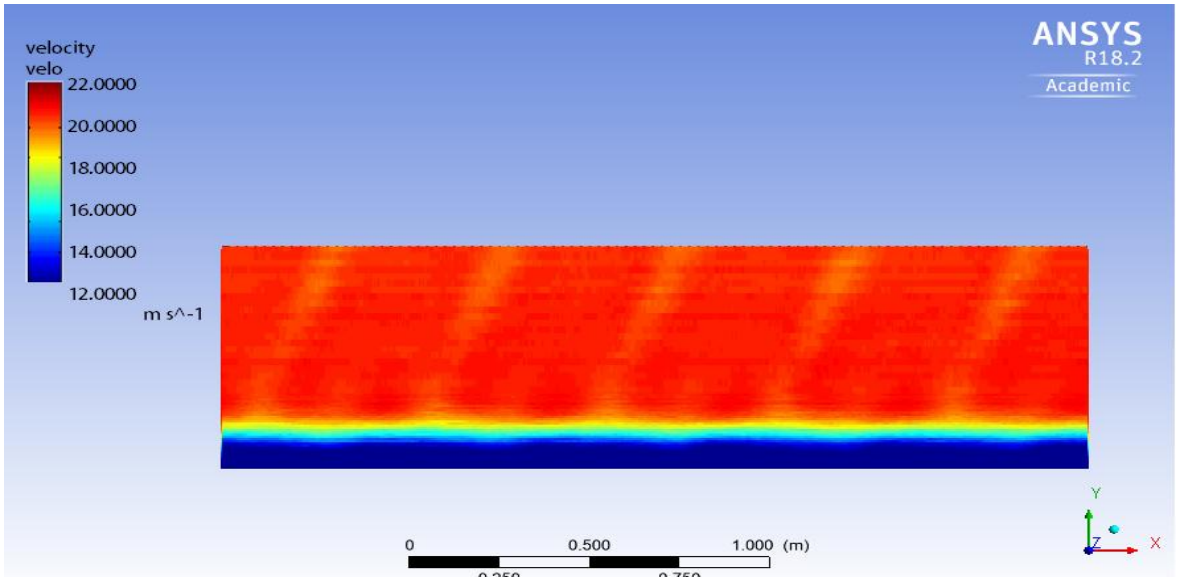

Figure 4.7 Velocity field for blade B, over suction surface, (ensemble average)

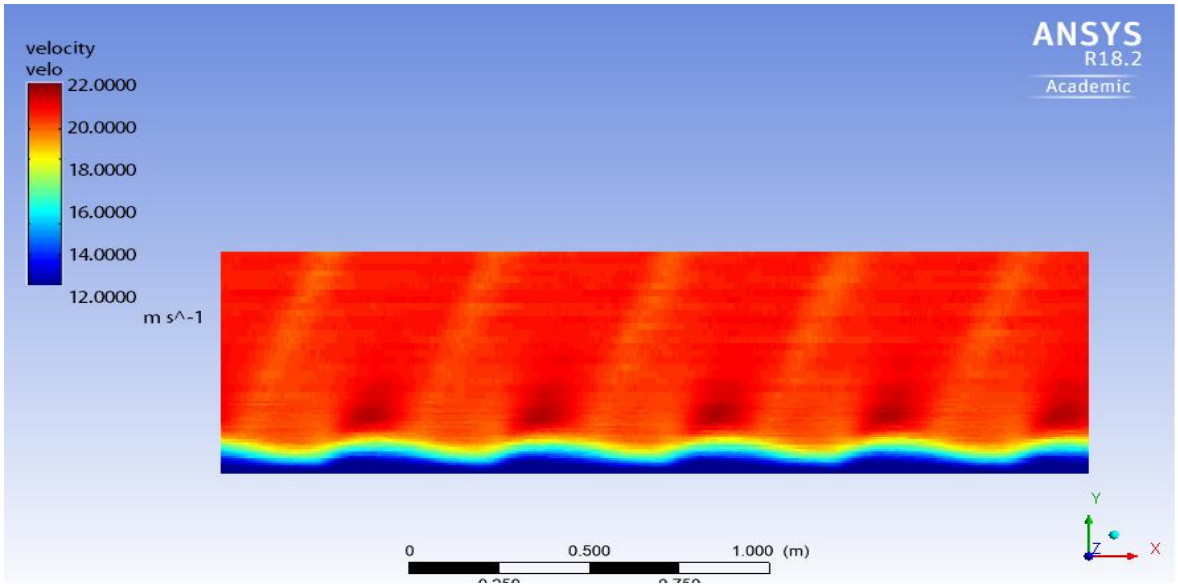

Figure 4.8 Velocity field for blade C, over suction surface, (ensemble average)

In Figure 4.6, 4.7 and 4.8 the ensemble averaged velocity field is plotted together with the momentum thickness for the three blades.

Regions of locally lower velocity can be observed in the free stream. These appear like yellow stripes (marked with W) and are believed to be the wakes, as confirmed later. Near the wall, a lower velocity region shows clearly the boundary layer.

Significant velocity fluctuation in the boundary layer is present on blades A and C their flow field appears to be very similar. On the other hand, on blade B, the wakes are still recognisable but the boundary layer looks very different, almost steady.

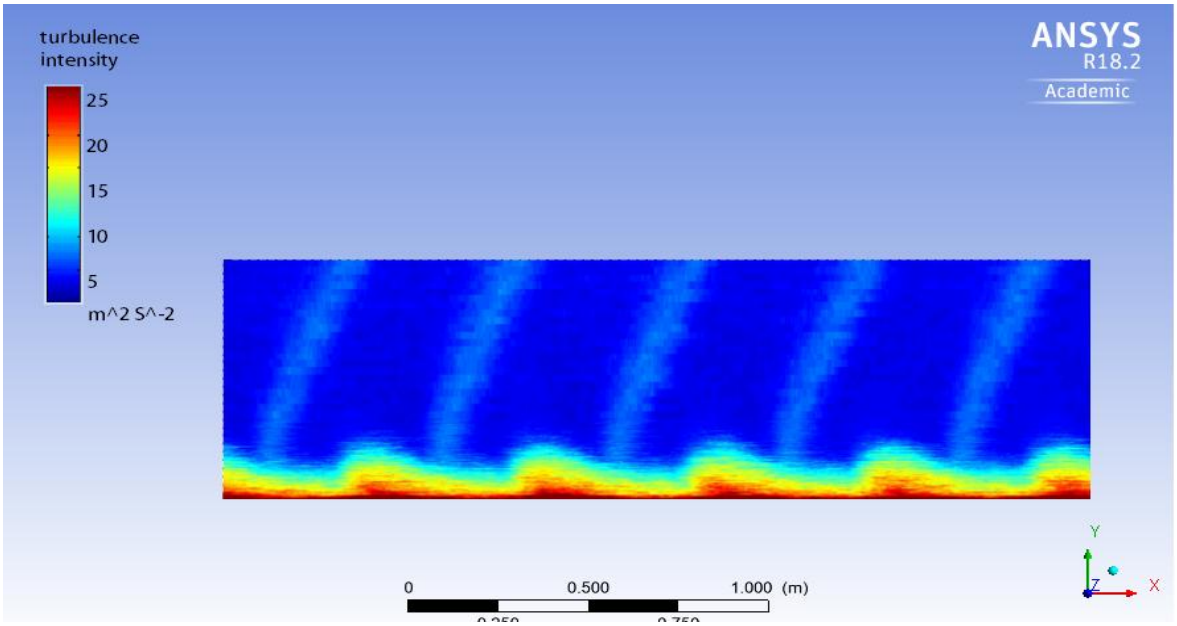

Figure 4.9 Turbulence level and momentum thickness for blade A

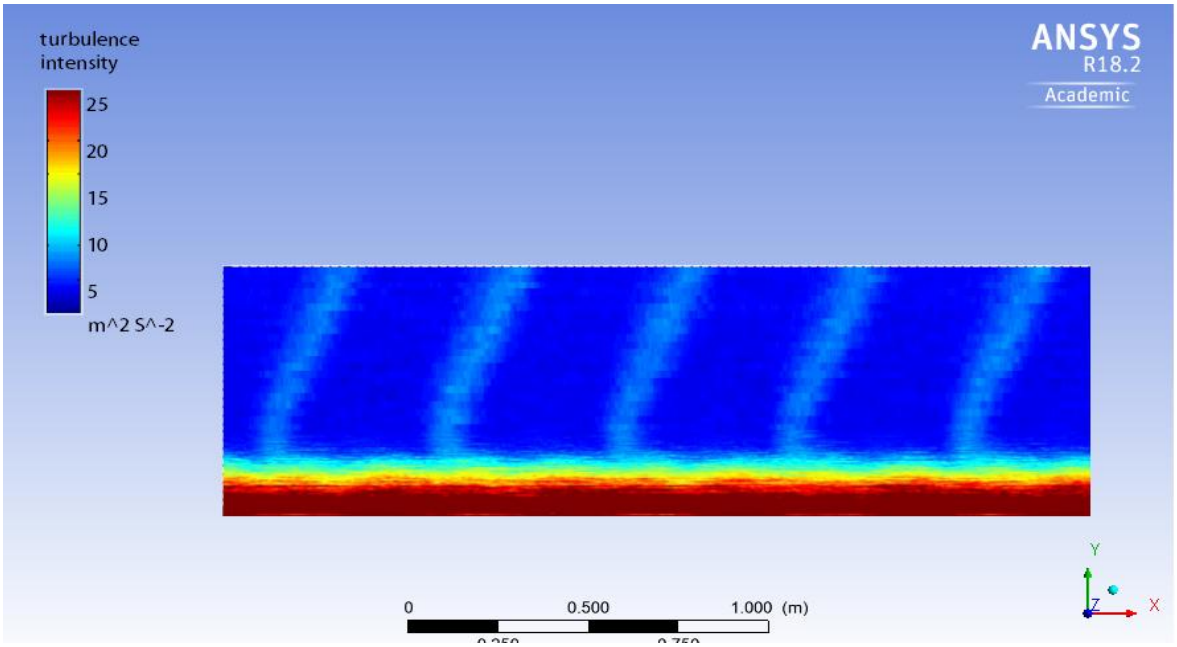

Figure 4.10 Turbulence level and momentum thickness for blade C

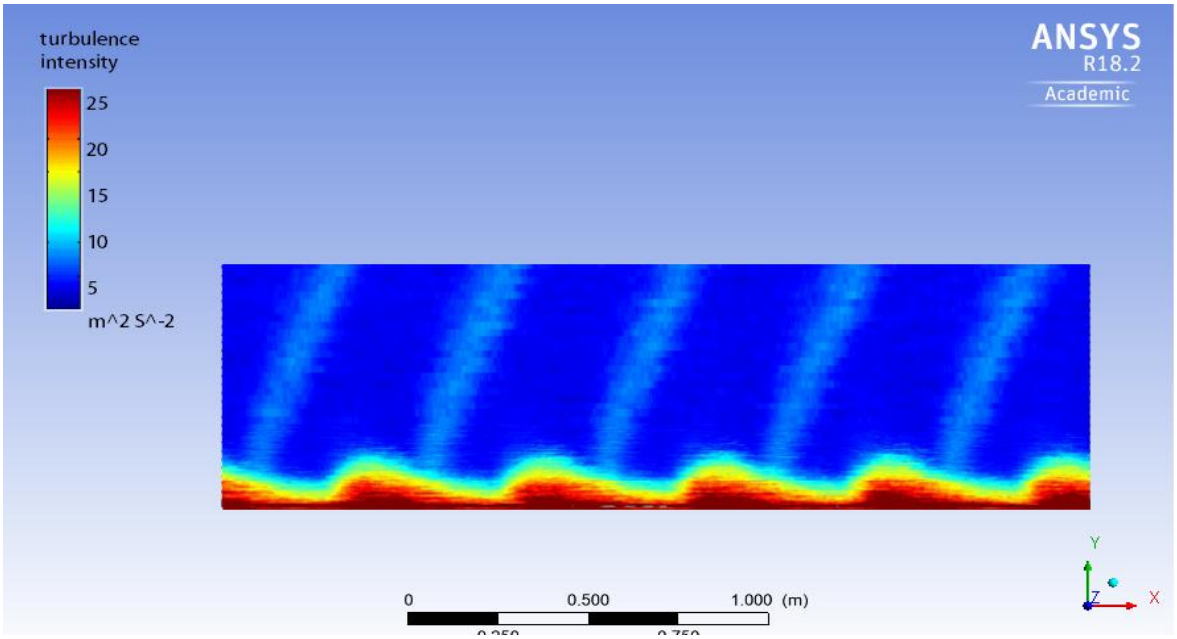

Figure 4.11 Turbulence level and momentum thickness for blade C

As further investigation, the turbulence of the flow inside the boundary layer has been computed. The wakes are again well visible. These are shown by a higher turbulence. These light blue stripes are in phase with the yellow stripes of previous plots, showing that the low velocity stripes observed were really the wakes.

A turbulence peak in the boundary layer is clearly identified in A and C. This structure appeared in the previous graphs as the low velocity region; it is in phase with the peak in the momentum thickness and is marked again with P. It is therefore clear that some loss generation mechanism must be associated with it, leading to the peak in the momentum thickness. The percentage turbulence level shows that the structures are not detached from the wall as they could appear in Figure 4.9, 4.10 and 4.11

Interestingly, the high values in θ_{TE} in A and C are not in phase in the wake: the wake has apparently no direct effect on it. However, the incoming wakes are believed to be the cause for the structures to appear.

The turbulent structures and the wakes are in phase at the leading edge. The structure P is induced by the wake as it hits the leading edge of the blade and convects behind it along the surface. The phase delay of the structure is given by its lower convective velocity. A slight difference in this phase delay is observed between the blade A and C, this might be the effect of a different convective velocity of the structure induced by the difference in the profile.

In blade B, the peak P cannot be identified. The different leading edge shape gives simply different flow physics of the boundary layer. However, due to the results shown in Figure 4.6, 4.7 and 4.8 (flow field perturbation). It is believed that a similar structure should be observable also in this case. Anyway, no appreciable peak in the trailing edge momentum thickness is present in phase with it.

Actually, in blade B, the small peaks in the trailing edge momentum thickness appear to be in phase with the wakes. This seems in contradiction with the comments above. However, the figures show different boundary layer characters in this case; a different

phase relation between θ_{TE} cannot therefore be excluded. Moreover, the same should actually happen in A and C, but since θ_{TE} oscillates widely, such a small variation is hard to recognize.

CHAPTER 5

CONCLUSION AND FUTURE SCOPE

Starting from the baseline blade (circular leading edge and 32˚ wedge angle), two new geometries have been designed. The new blades have a 15˚ wedge angle and a circular and an elliptic (3:1) leading edge, respectively. Their leading edge geometry is therefore more representative of a real engine blade.

The three test cases are:

A: 32° wedge angle, circular leading edge;

B: 15° wedge angle, circular leading edge;

C: 15° wedge angle, elliptic (3:1) leading edge.

It found that the loss coefficients Y_p for the three blades are:

Blade A: Y_p=2.5%

Blade B: Y_p=3.3%

Blade C: Y_p=2.5%

Clearly, the highest loss value is associated with the widest and deepest wake: B. A and C have similar wake profiles and therefore similar loss.

A CFD analysis using the two dimensional and 3D steady blade cascade has been performed on the three test cases. A low speed, single stage, axial flow compressor. The C_p distribution has been measured using rake with a very fine resolution at the leading edge, to capture the suction spike and eventually the separation bubble, allowing to measure the wake of the test blades and to get a time averaged loss coefficientY_P. Finally the boundary layer at the trailing edge, providing an unsteady measurement of the

trailing edge momentum thickness. With a 15° wedge angle, a comparison between the elliptic and the circular leading edge has shown significant advantages for the elliptic shape. Y_P is 3.3% for blade B and only 2.5% for C, that is about 25% less. The trailing edge momentum thickness θ_{TE} drops from 1.43 mm up to 1.02 mm (mean) for C. The behavior and performances of the high wedge angle blade A (is Y_P 2.5% and the mean θ_{TE} is 1.10 mm) are very similar to those of blade C.

5.1 FURTHER INVESTIGATION ON THE PRESENT TEST BLADES

The results of this work are consistent with those presented in [9] and [10]. Those results are based on measurements done on the baseline blade A. Similar results are to be expected on blade C, some difference in the intensity and convective velocity of the boundary layer structures are likely. Blade B showed the worst performances. From this point of view, further investigations seem to be useless. But, on the other hand, blade B shows a completely different physics: a different behavior of the boundary layer and probably different mechanisms of wake-leading edge interaction. For this reason, additional studies could bring interesting new results and let us gain some more understanding of the physics of the problem.

5.2 NEW GEOMETRIES

The goal of this project was not to design the best possible leading edge; no optimization has been performed and the chosen leading edge geometries were rather simple. This has shown a good potential for improvement. Much other geometry could be tested: ellipses with different axes ratio, parabolic or hyperbolic leading edges, and even asymmetric leading edges. This may lead to the final goal of designing optimized geometries with better performances.

For example: since the wake causes generally higher incidence, the leading edge might be slightly drooped. This may lead to an improved behavior when the wake hits the leading edge. However, manufacturing issues must be kept in mind. Compressor blades are usually relatively small and the manufacturing of rather complicated geometries

might end up being almost impossible. The effect of erosion during the service must be also taken into account.

5.3 THREE DIMENSIONAL PHENOMENA

The flow visualization results show clearly that the modification of the leading edge could lead to some initially unexpected phenomena like for example endwall separations. This represented rather a problem for this work, since the task was a two dimensional analysis at mid height, and has been solved unsealing the hub gap.

It has been observed that the tripped boundary layer of blade B was more prone to separate (higher shape factor). The result was a significantly bigger corner stall. If the observed phenomena can be generalized or if it is specific for the tested geometry is still questionable; however, a deeper investigation of the effect of the leading edge geometry on the three dimensional behavior of the flow (and specifically on the endwall flows) might be worth doing.

REFERENCES

1. Hinze, J. O. (1975). Turbulence (No. BOOK). McGraw-Hill.
2. Fluent, A. (2009). 12.0 Theory Guide. Ansys Inc, 5(5).
3. Dreese, J. (2000). Aero Basics and Design FOIL User Guide. Capitola, California.
4. Hepperle, M. (2011). JAVAFOIL user's guide.
5. Yahya, S. M. (1987). Turbines compressors and fans. Tata McGraw-Hill Education.
6. Oh, H. W., Yoon, E. S., & Chung, M. K. (1997). An optimum set of loss models for performance prediction of centrifugal compressors. Proceedings of the Institution of Mechanical Engineers, Part A: Journal of Power and Energy, 211(4), 331-338.
7. Summerfield, L. R. (1995). U.S. Patent No. 5,440,490. Washington, DC: U.S. Patent and Trademark Office.
8. Mattingly, J. D. (2006). Elements of propulsion: gas turbines and rockets. American Institute of Aeronautics and Astronautics.
9. Korpela, S. A. (2012). Principles of turbomachinery. John Wiley & Sons.
10. Gbadebo, S. A., Cumpsty, N. A., & Hynes, T. P. (1990). Control of three-dimensional separations in axial compressors by tailored boundary layer suction. Journal of turbomachinery, 130(1), 011004.
11. Arena, A. V., & Mueller, T. J. (1980). Laminar separation, transition, and turbulent reattachment near the leading edge of airfoils. AIAA journal, 18(7), 747-753.Bolger,
12. Walraevens, R. E., & Cumpsty, N. A. (1995). Leading edge separation bubbles on turbomachine blades. Journal of Turbomachinery, 117(1), 115-125.

13. Tain, L., & Cumpsty, N. A. (2000). Compressor blade leading edges in subsonic compressible flow. Proceedings of the Institution of Mechanical Engineers, Part C: Journal of Mechanical Engineering Science, 214(1), 221-242.

14. J. J. (1999). Three dimensional design of compressor blades (Doctoral dissertation, University of Cambridge).

15. Wheeler, A. P., Miller, R. J., & Hodson, H. P. (2007). The effect of wake induced structures on compressor boundary-layers. Journal of Turbomachinery, 129(4), 705-712.

16. Wheeler, A. P., Miller, R. J., & Hodson, H. P. (2006). The effect of wake induced structures on compressor boundary-layers. Journal of Turbomachinery, 129(4), 705-712.

17. Wheeler, A. P., Miller, R. J., & Hodson, H. P. (2007). The effect of wake induced structures on compressor boundary-layers. Journal of Turbomachinery, 129(4), 705-712.

18. Wilcox, D. C. (1993). Comparison of two-equation turbulence models for boundary layers with pressure gradient. AIAA journal, 31(8), 1414-1421.

19. Chen, C.J, and Jaw, S.Y. [1998][10] summarized

20. Ahmed, N., Yilbas, B. S., & Budair, M. O. (1998). Computational study into the flow field developed around a cascade of NACA 0012 airfoils. Computer methods in applied mechanics and engineering, 167(1-2), 17-32.

21. YOUNGREN, H., & Drela, M. (1998). A User Guide to Mises 2.53Place, J. M. M. (1997). Three-dimensional flow in core compressors (Doctoral dissertation, University of Cambridge).

22. Zachos, P. K., Grech, N., Charnley, B., Pachidis, V., & Singh, R. (2011). Experimental and numerical investigation of a compressor cascade at highly

negative incidence. Engineering Applications of Computational Fluid Mechanics, 5(1), 26-36.

23. Goodhand, M. N. (2011, June). Laminar flow compressor blades. In 9th Osborne Reynolds Colloquium and Research Student Award, Department of Aeronautics-Imperial College London.

24. Adeniyi, A. A., Mohammed, A., & Emmanuel, S. O. (2012). CFD Modelling of Wakes on Cascade Compressor Blades. International Journal of Advances in Science and Technology, 4(2).

25. Azim, R., Hasan, M. M., & Ali, M. (2015). Numerical investigation on the delay of boundary layer separation by suction for NACA 4412. Procedia Engineering, 105, 329-334.

26. Zhang, H., Wu, Y., Li, Y., & Lu, H. (2015). Experimental investigation on a high subsonic compressor cascade flow. Chinese Journal of Aeronautics, 28(4), 1034-1043.

27. Peyvan, A., & Benisi, A. H. (2016). Axial-Flow Compressor Performance Prediction in Design and Off-Design Conditions through 1-D and 3-D Modeling and Experimental Study. Journal of Applied Fluid Mechanics, 9.

28. Bai, T., Liu, J., Zhang, W., & Zou, Z. (2014). Effect of surface roughness on the aerodynamic performance of turbine blade cascade. Propulsion and Power Research, 3(2), 82-89.

29. Zhang, H., Chen, S., Gong, Y., & Wang, S. (2018). A comparison of different unsteady flow control techniques in a highly loaded compressor cascade. Proceedings of the Institution of Mechanical Engineers, Part G: Journal of Aerospace Engineering, 0954410018770492.

30. Ghazanfari, B., Nili-Ahmadabadi, M., Torabi-Farsani, A., & Noorsalehi, M. H. (2018). Numerical study of camber and stagger angle effects on the aerodynamic

performance of tandem-blade cascades. Propulsion and Power Research, 7(1), 30-42.

31. Borello, D., Hanjalic, K., & Rispoli, F. (2007). Computation of tip-leakage flow in a linear compressor cascade with a second-moment turbulence closure. International Journal of Heat and Fluid Flow, 28(4), 587-601.

32. Lin, S. C., & Huang, C. L. (2002). An integrated experimental and numerical study of forward–curved centrifugal fan. Experimental thermal and fluid science, 26(5), 421-434.

33. Widmann, J. F., Charagundla, S. R., & Presser, C. (2000). Aerodynamic study of a vane-cascade swirl generator. Chemical Engineering Science, 55(22), 5311-5320.

34. Christophel, J. R., Thole, K. A., & Cunha, F. J. (2004, January). Cooling the Tip of a Turbine Blade Using Pressure Side Holes: Part 1—Adiabatic Effectiveness Measurements. In ASME Turbo Expo 2004: Power for Land, Sea, and Air (pp. 263-271). American Society of Mechanical Engineers.

35. Yen, S. C., & Liu, J. H. (2007). PIV measurements of exit flow field of centrifugal fans with conditional sampling. Journal of Marine Science and Technology, 15(3), 232-240.

APPENDIX 1

1.1 Surface Pressure Coefficient at Low Reynolds Number

Surface Pressure Coefficient						X/C
Blade A		Blade B		Blade C		
Pressure Surface	Suction Surface	Pressure Surface	Suction Surface	Pressure Surface	Suction Surface	
2.245	-1.048	2.417	-0.9303	2.045	-0.3798	0.05
1.194	-0.5875	1.172	-0.6077	1.195	-0.5831	0.1
2.011	-0.4223	2.042	-0.4679	2.074	-0.4015	0.15
1.91	-0.31	1.821	-0.359	1.744	-0.3191	0.2
1.554	-0.2315	1.571	-0.306	1.494	-0.2694	0.25
1.341	-0.3934	1.385	-0.4065	1.373	-0.4159	0.3
0.9626	-0.271	0.9702	-0.3931	0.941	-0.2471	0.35
0.712	-0.3489	0.749	-0.331	0.719	-0.323	0.4
0.7402	-0.3142	0.8067	-0.3199	1.005	-0.2857	0.45
0.7351	-0.32	0.8021	-0.3193	0.7527	-0.3069	0.5
0.8746	-0.2907	0.7743	-0.3224	0.7078	-0.3315	0.55
0.757	-0.3065	0.7479	-0.5029	0.6429	-0.1676	0.6
0.5321	-0.3103	0.5249	-0.341	0.4352	-0.2152	0.65
0.6296	-0.127	0.6514	-0.166	0.4262	-0.264	0.7
0.4229	-0.2487	0.4118	-0.2186	0.4215	-0.2285	0.75
0.3875	-0.1494	0.3171	-0.2009	0.3462	-0.03938	0.8
0.189	-0.105	0.1504	-0.3151	0.1562	-0.1124	0.85
0.1498	-0.079	0.04986	-0.1276	-0.1454	-0.4547	0.9
-0.00896	-0.00852	0.04915	0.04349	0.04976	-0.1876	0.95

1.2 Surface Pressure Coefficient at High Reynolds Number

Surface Pressure Coefficient	

Blade A		Blade B		Blade C		
Pressure Surface	Suction Surface	Pressure Surface	Suction Surface	Pressure Surface	Suction Surface	
2.016	-0.5102	1.298	-1.047	1.748	-1.693	0.05
1.095	-0.3025	1.03	-0.3385	1.035	-0.0257	0.1
1.107	-0.0289	0.67	-0.3571	1.249	-0.3565	0.15
1.119	-0.0828	0.843	-0.3833	0.95	-0.2074	0.2
0.9746	-0.1038	0.9546	-0.4358	0.91	-0.2082	0.25
0.8437	-0.0846	1.005	-0.481	0.89	-0.2047	0.3
0.7797	-0.03675	0.9735	-0.4161	0.87	-0.2036	0.35
0.912	-0.0713	0.9023	-0.472	0.5731	-0.2409	0.4
0.8753	-0.02383	0.6371	-0.4651	0.584	-0.2508	0.45
0.5887	-0.02801	0.5704	-0.631	0.5412	-0.2389	0.5
0.609	-0.0349	0.5098	-0.487	0.385	-0.2355	0.55
0.6137	-0.2583	0.4084	-0.4609	0.3097	-0.2639	0.6
0.4814	-0.2087	0.46	-0.5118	0.2915	-0.188	0.65
0.4369	-0.378	0.2504	-0.5976	0.2797	-0.17	0.7
0.3819	-0.2073	0.259	-0.5803	0.2642	-0.22	0.75
0.2286	-0.2179	0.2633	-0.7017	-0.01647	-0.087	0.8
0.1485	-0.3624	0.2492	-0.4078	-0.03996	-0.06014	0.85
0.2712	-0.1891	0.2393	-0.312	-0.082	-0.263	0.9
0.01781	0.035	0.09436	0.0906	-0.68	-0.6085	0.95

1.3 Profile loss calculation

Profile Loss Calculation			X/C
Blade A	Blade B	Blade C	
0.9997	0.6332	0.9997	0.01
0.778	0.2419	0.8293	0.02
0.404	0.04652	0.4763	0.03

0.03968	-0.009956	0.08434	0.04
-0.01763	-0.01041	-0.02968	0.05
-0.01058	-0.006831	-0.02855	0.06
-0.003908	-0.004003	-0.01814	0.07
0.0007421	-0.00371	-0.009853	0.08
0.0002503	-0.00404	-0.007333	0.09
-0.000387	-0.00426	-0.00723	0.1
-0.0002453	-0.004279	-0.005123	0.11
0.00005966	-0.004415	-0.004275	0.12
-0.0001509	-0.004469	-0.003977	0.13
-0.000216	-0.004479	-0.003936	0.14
-0.0002569	-0.004699	-0.003928	0.15
-0.0002159	-0.005217	-0.003949	0.16
-0.00003377	-0.005645	-0.003773	0.17
-0.0001411	-0.005553	-0.003841	0.18
-0.0002032	-0.00514	-0.003872	0.19
-0.0001596	-0.004905	-0.003762	0.2
-0.0001482	-0.005107	-0.003652	0.21
-0.00003088	-0.005542	-0.003467	0.22
-0.0001238	-0.005825	-0.003511	0.23
-0.00009409	-0.005891	-0.003442	0.24
-0.0001666	-0.005789	-0.003516	0.25
0.000004437	-0.005615	-0.00338	0.26
0.00003413	-0.0054	-0.003403	0.27
0.00008014	-0.005449	-0.003344	0.28
0.00005958	-0.005892	-0.003421	0.29
-0.0002295	-0.006556	-0.003712	0.3
0.0001437	-0.006973	-0.003301	0.31
-0.0001414	-0.007256	-0.00353	0.32
-0.0001314	-0.007088	-0.003513	0.33

0.0003301	-0.006615	-0.003066	0.34
0.00002128	-0.006042	-0.003451	0.35
0.0001477	-0.00573	-0.00342	0.36
-0.0000321	-0.006102	-0.003718	0.37
0.0003309	-0.007564	-0.00358	0.38
0.0001591	-0.009744	-0.004514	0.39
-0.0001038	-0.01489	-0.005394	0.4
-0.00003265	-0.02298	-0.005886	0.41
0.0005349	-0.03282	-0.005963	0.42
0.00122	-0.032	-0.005752	0.43
0.0007575	0.01053	-0.009641	0.44
-0.00713	0.1259	-0.01994	0.45
-0.01162	0.3101	-0.02151	0.46
0.08533	0.6042	0.08853	0.47
0.3065	0.8304	0.29	0.48
0.4698	0.9784	0.449	0.49
0.85	0.3721	0.82	0.5
0.84	0.1365	0.89	0.51
0.5707	0.004788	0.6024	0.52
0.2525	-0.01292	0.3089	0.53
0.0008892	-0.006869	-0.007085	0.54
-0.01159	-0.004039	-0.03389	0.55
-0.00225	-0.004159	-0.02232	0.56
0.003742	-0.004377	-0.01167	0.57
0.004373	-0.00429	-0.006703	0.58
0.003433	-0.004102	-0.006256	0.59
0.002592	-0.004031	-0.006029	0.6
0.001677	-0.004069	-0.006344	0.61
0.00194	-0.004188	-0.005527	0.62
0.001669	-0.004469	-0.005293	0.63

0.0018	-0.005043	-0.004835	0.64
0.001841	-0.005553	-0.004548	0.65
0.001742	-0.005639	-0.004529	0.66
0.001411	-0.005144	-0.004911	0.67
0.001476	-0.004719	-0.004882	0.68
0.001436	-0.004772	-0.004849	0.69
0.00149	-0.005074	-0.004782	0.7
0.001491	-0.005253	-0.004751	0.71
0.001572	-0.005408	-0.004545	0.72
0.001557	-0.005333	-0.004454	0.73
0.00159	-0.005048	-0.004448	0.74
0.001657	-0.004928	-0.004487	0.75
0.001637	-0.005216	-0.004545	0.76
0.001609	-0.005683	-0.00449	0.77
0.001642	-0.006298	-0.004384	0.78
0.001643	-0.006518	-0.004294	0.79
0.001577	-0.006281	-0.004293	0.8
0.001669	-0.006011	-0.00429	0.81
0.001743	-0.005768	-0.004347	0.82
0.001662	-0.005697	-0.00459	0.83
0.001744	-0.006023	-0.004776	0.84
0.001842	-0.006295	-0.005023	0.85
0.00207	-0.006524	-0.005312	0.86
0.002153	-0.006552	-0.005676	0.87
0.00247	-0.008625	-0.005964	0.88
0.002533	-0.01344	-0.006613	0.89
0.002585	-0.02175	-0.008541	0.9
0.002639	-0.0205	-0.009794	0.91
0.004168	-0.00009332	-0.009607	0.92
0.005048	0.05956	-0.01309	0.93

0.002245	0.218	-0.02205	0.94
-0.001612	0.5172	-0.02536	0.95
0.02842	0.7733	0.07747	0.96
0.1992	0.9711	0.2424	0.97
0.3881	0.9998	0.4005	0.98

APPENDIX 2

2.1 INTRODUCTION TO JAVAFOIL

JavaFoil implements a classical panel method with linearly varying vorticity distribution. This is somewhere between the panel methods in XFOIL (constant vorticity per panel) and Epplers PROFIL code (parabolic variation of vorticity). The resulting equation system consists therefore of a (# of panels +1)² sized matrix and two right hand sides. These are for 0° and 90° angle of attack and can be solved for the two corresponding vorticity distributions efficiently. The vorticity distribution for any arbitrary angle of attack is then derived from these two solutions (remember that potential theory is linear and allows for superposition). There is no interaction with the boundary layer, as in XFOIL, though.

$$\begin{bmatrix} C_{1,1} & \cdots & C_{N+1,1} \\ \vdots & \ddots & \vdots \\ C_{1,N} & \cdots & C_{N+1,N} \\ 1 & \cdots 0 \cdots & 1 \end{bmatrix} \cdot \begin{bmatrix} \gamma_{1,0°} & \gamma_{1,90°} \\ \gamma_{2,0°} & \gamma_{2,90°} \\ \vdots & \vdots \\ \gamma_{N+1,0°} & \gamma_{N+1,90°} \end{bmatrix} = \begin{bmatrix} RHS_{1,0°} & RHS_{1,90°} \\ RHS_{2,0°} & RHS_{2,90°} \\ \vdots & \vdots \\ RHS_{N+1,0°} & RHS_{N+1,90°} \end{bmatrix}$$

2.2 Critical Pressure Coefficient

When the local pressure somewhere on the airfoil surface drops below the critical pressure, the flow speed exceeds the speed of sound. When supersonic speed is exceeded anywhere on the surface, the character of the flow may change dramatically. In most cases pressure recovery from supersonic to subsonic velocities (from Cp < Cp,crit to Cp > Cp, crit) is to leading abrupt recompression with shocks. The analysis of these flow fields requires more complex methods, capable of handling compressible flows (e.g. by solving the full compressible potential equations or by solving the Euler equations).

In JavaFoil, the critical pressure coefficient is calculated from the relation

$$C_{p,crit} = \frac{2}{\kappa \cdot M_\infty^2} \cdot \left(\left(\frac{2}{\kappa+1} \cdot \left(1 + \frac{\kappa-1}{2} \cdot M_\infty^2 \right) \right)^{\frac{\kappa}{\kappa-1}} - 1 \right)$$

(Küchemann, „The Aerodynamic Design of Aircraft“, p.115).

In terms of the velocity ratio the critical limit is found from

$$\left(\frac{v}{v_\infty} \right)_{crit} = \sqrt{1 + 2 \cdot \frac{1 + M_\infty^2}{(\kappa+1) \cdot M_\infty^2}}$$

2.3 Compressibility Corrections

There are different ways to correct incompressible flow results for compressibility effects. One should keep in mind that these are only corrections – they can never produce the correct physical effects. Therefore the applicability of all compressibility corrections is limited to cases where the local flow velocity (which can be much higher than the onset flow velocity) is well beyond the speed of sound. In practical application one can use such corrections up to maybe Mach = 0.6, but the error grows rapidly when Mach exceeds 0.8. In *JavaFoil*, the panel analysis is always running on the given airfoil shape – it is never geometrically distorted. Compressibility corrections are applied later to the local surface velocities according to the Kàrmàn-Tsien approximation (usually written for Cp)

$$\left(\frac{v}{v_\infty} \right)_{comp.} = \left(\frac{v}{v_\infty} \right)_{inc.} \cdot \frac{1 - \frac{M_\infty^2}{2 - M_\infty^2}}{1 - \frac{M_\infty^2}{2 - M_\infty^2} \cdot \left(\frac{v}{v_\infty} \right)_{inc.}^2}$$

2.4 Boundary Layer Analysis

The boundary layer analysis module implements an integral boundary layer integration scheme following publications by Prof. R. Eppler. Note: the local skin friction

coefficient as given on the Boundary Layer card is twice the value as used by Eppler to follow the more common convention .

In *JavaFoil* there is no interaction between the boundary layer and the external flow, as in *XFOIL,* though. Therefore largely separated flows cannot be analyzed – a short flow separation (Ssep < 10%) at the trailing edge does not affect the results very much. Also laminar separation bubbles are not modeled; when laminar separation is detected the code switches to turbulent flow.

2.4 Correction of Lift for given Aspect Ratio and Mach number

For a given angle of attack, a 3D wing of finite aspect ratio produces less lift than the 2D airfoil section, which corresponds to an infinite aspect ratio. Another correction has to be applied when the Mach number is larger than zero. In subsonic flight more lift is produced when the Mach numbers is increased.

The following correction is applied to the lift coefficient of a 2D airfoil C_l in order to approximate the lift coefficient C_l of a 3D wing in compressible flow. The correction is divided into two regimes of aspect ratios.

For small aspect ratios ($\Lambda<4$) the following formula is used:

$$C_L = \frac{C_\ell}{\sqrt{1-M_\infty^2+\left(\frac{2\cdot\pi}{\Lambda\cdot\pi}\right)^2}+\frac{2\cdot\pi}{\Lambda\cdot\pi}}$$

If the aspect ratio is larger, $\Lambda \geq 4$, the simplified approximation is applied:

$$C_L = \frac{C_\ell}{\sqrt{1-M_\infty^2}+\frac{2\cdot\pi}{\Lambda\cdot\pi}}$$

2.4 Implementation in Javafoil

```
public final static double LiftForAspectRatio(double dCl,
                                               double dAspectRatio,
                                               double dMachNumber)
    {
        double dReturn = dCl;

        // correction for finite wings
        if (dAspectRatio > 0.1)
        {
            // Source: Anderson, "Aircraft Performance and Design"
            // lift gradient reduction factor
            // a 0 / (pi*AR)
            double dGradientRatio = 2.0 * Math.PI / (Math.PI *
                                    dAspectRatio);
            if (dAspectRatio < 4.0)
            {
                // low aspect ratio, compressible (Anderson [2.18b])
                dReturn /=
                        (Math.sqrt(1.0 - Math.pow(dMachNumber, 2.0) +
                                  Math.pow(dGradientRatio, 2.0)) +
                         dGradientRatio);
            }
            else
            {
                // high aspect ratio, compressible (Anderson [2.16])
                dReturn /=
                        (Math.sqrt(1.0 - Math.pow(dMachNumber, 2.0)) +
                         dGradientRatio);
            }
        }
        return (dReturn);
    }
```

Thesis

ORIGINALITY REPORT

9%	%	9%	%
SIMILARITY INDEX	INTERNET SOURCES	PUBLICATIONS	STUDENT PAPERS

PRIMARY SOURCES

1	Ramin K. Rahmani, Anahita Ayasoufi, Theo G. Keith. "A Numerical Study of Turbulent Flow in Helical Static Mixers", Volume 2: Fora, 2006 Publication	1%
2	Ahmad, Salman. "Effect of Forward Sweep on the Performance of an Axial Blower", Universität Karlsruhe, 2010. Publication	1%
3	S. Prem Kumar, M. Dev Anand, P. Gopu. "Heat transfer and friction factor characteristics of nano fluids in the circular straight channel under constant heat flux method", 2014 International Conference on Control, Instrumentation, Communication and Computational Technologies (ICCICCT), 2014 Publication	1%
4	Valery Ponyavin, Yitung Chen, Darrell W. Pepper, Hsuan-Tsung Hsieh. "Numerical Modeling of the Turbulent Supersonic Flow Over a Backward Facing Step", Fluids Engineering, 2004	<1%

Publication

5	Al-Soudani , Yousef Moh'd. "Effects of Wake Splitter Plates on the Flow past a Circular Cylinder at Supercritical Reynolds Number = تأثيرات الصفيحة الفاصلة الخلفية على التدفق حول أسطوانة دائرية عند رقم رينولدز ما بعد الحرج", University of Jordan Publication	<1%
6	Satyam Panchal, Vijay Mayavanshi. "Experimental study of flow through compressor Cascade", Case Studies in Thermal Engineering, 2017 Publication	<1%
7	Khalil, Essam, Gamal Elhariry, and Ahmed Mostafa. "Effect of Air Curtain on Flow Regimes and Heat Transfer characteristics in a Refrigerated Cold Room", 51st AIAA Aerospace Sciences Meeting including the New Horizons Forum and Aerospace Exposition, 2013. Publication	<1%
8	Jiang, . "Numerical Treatment of Boundary Conditions", Chapman & Hall/CRC Numerical Analy & Scient Comp Series, 2009. Publication	<1%
9	Zhengping Zou, Songtao Wang, Huoxing Liu, Weihao Zhang. "Axial Turbine Aerodynamics for Aero-engines", Springer Nature, 2018 Publication	<1%

10	Wei-chao Yang, Li-min Peng, Li-chuan Wang. "Computation Simulation on Aerodynamic Characteristic of PSD in Subway Platform", 2009 International Conference on Computer Engineering and Technology, 2009 Publication	<1%
11	Boyce, Meherwan P.. "Axial-Flow Compressors", Gas Turbine Engineering Handbook, 2012. Publication	<1%
12	I. Lee, , S. Lee, G. Kim, J. Sung, S. Sung, and Y. Yoon. "PIV VERIFICATION OF GREENHOUSE VENTILATION AIR FLOWS TO EVALUATE CFD ACCURACY", Transactions of the ASAE, 2005. Publication	<1%
13	"CFD Techniques and Thermo-Mechanics Applications", Springer Nature, 2018 Publication	<1%
14	Mishra, Dipti Prasad, Mihir Kumar Samantaray, and Sukanta K. Dash. "Maximum air entrainment into a mixing pipe through optimum design", Ships and Offshore Structures, 2014. Publication	<1%
15	de Lieto Vollaro, Andrea, Giuseppe de Simone, Roberto Romagnoli, Andrea Vallati, and	<1%

Simone Botillo. "Numerical Study of Urban Canyon Microclimate Related to Geometrical Parameters", Sustainability, 2014.
Publication

---

16 F. Gu. "CFD Simulation of Liquid Film Flow on Inclined Plates", Chemical Engineering & Technology, 10/2004 <1%
Publication

---

17 Ebiana, Asuquo, and Praveen Gidugu. "Effect of Adding a Regenerator to Kornhauser's MIT "Two-Space" (Gas-Spring + Heat Exchanger) Test Rig", 6th International Energy Conversion Engineering Conference (IECEC), 2008. <1%
Publication

---

18 Ji, Yingfeng, Ryoichi S. Amano, and Ronald A. Perez. "Modeling and Control of Underwater Pan/Tilt Camera Tracking System", Volume 2 29th Computers and Information in Engineering Conference Parts A and B, 2009. <1%
Publication

---

19 Liesner, Karsten, Robert Meyer, Matthias Lemke, Christoph Gmelin, and Frank Thiele. "On the Efficiency of Secondary Flow Suction in a Compressor Cascade", Volume 7 Turbomachinery Parts A B and C, 2010. <1%
Publication

---

20 Xiaochang Li, Ye Gao. "Methods of simulating

	large-scale rod bundle and application to a 17×17 fuel assembly with mixing vane spacer grid", Nuclear Engineering and Design, 2014 Publication	<1%
21	Kim, Jongmin, and Nikhil Koratkar. "Effect of Unsteady Blade Motion on the Aerodynamic Performance of Micro-Rotorcraft", 44th AIAA/ASME/ASCE/AHS/ASC Structures Structural Dynamics and Materials Conference, 2003. Publication	<1%
22	Joel H. Ferziger. "Introduction to Numerical Methods", Computational Methods for Fluid Dynamics, 2002 Publication	<1%
23	Song, Yin, Chun-Wei Gu, and Yao-Bing Xiao. "Numerical and Theoretical Investigations Concerning the Continuous-Surface-Curvature Effect in Compressor Blades", Energies, 2014. Publication	<1%
24	Srinivasan C. Rasipuram, Karim J. Nasr. "Effect of Angle and Separation Distance on Heat Transfer on an Inclined Surface Subject to Airflow", Heat Transfer, Volume 1, 2003 Publication	<1%
25	R. Ravindran. "The influence of the motion of a rotor grid on a stator grid", Acta Mechanica,	<1%

03/1981
Publication

26	Amano, Ryoichi, Pradeep Rohatgi, Dejan Ristic, Pradeep Mohandas, and Zhenyu Xu. "Numerical Modeling in Lens^tm Process", 9th AIAA/ASME Joint Thermophysics and Heat Transfer Conference, 2006. Publication	<1%
27	O. Lotfi, J. A. Teixeira, P. C. Ivey, G. Sheard, I. R. Kinghorn. "Aerodynamic Optimization of Industrial Fan Blade Cascades", Volume 6: Turbo Expo 2005, Parts A and B, 2005 Publication	<1%
28	"Low Reynolds Number Aerodynamics", Springer Nature, 1989 Publication	<1%
29	"CFD Analysis on the Air-Side Thermal-Hydraulic Performance of Multi-Louvered Fin Heat Exchangers at Low Reynolds Numbers", Energies, 2017 Publication	<1%
30	KHAN, FARUKH, and THOMAS MUELLER. "Tip vortex/airfoil interaction for a canard/wing configuration at low Reynolds numbers", 27th Aerospace Sciences Meeting, 1989. Publication	<1%

Akhilesh Arora. "Energy and exergy analysis of

31	a combined transcritical CO_2 compression refrigeration and single effect H_{2O}-LiBr vapour absorption system", International Journal of Exergy, 2011 Publication	<1%
32	Mihić, Stefan D., Sorin Cioc, Ioan D. Marinescu, and Michael C. Weismiller. "Detailed Study of Fluid Flow and Heat Transfer in the Abrasive Grinding Contact Using Computational Fluid Dynamics Methods", Journal of Manufacturing Science and Engineering, 2013. Publication	<1%
33	Chen, Ping-Ping, Wei-Yang Qiao, Karsten Liesner, and Robert Meyer. "Effect of Segment Endwall Boundary Layer Suction on Compressor 3D Corner Separation", Volume 2A Turbomachinery, 2015. Publication	<1%
34	Fath, H.E.S.. "Micro-climatic environmental conditions inside a greenhousewith a built-in solar distillation system", Desalination, 20050120 Publication	<1%
35	Anupam Dewan. "Tackling Turbulent Flows in Engineering", Springer Nature, 2011 Publication	<1%
36	M. Tutar. "The Computational Modeling of	<1%

Transitional Flow through a Transonic Linear Turbine: Comparative Performance of Various Turbulence Models", Numerical Heat Transfer Part A Applications, 01/2010
Publication

---

37 Chen, Jen-Ping, Benjamin P. Johnson, Michael D. Hathaway, and Robert S. Webster. "Flow Characteristics of Tip Injection on Compressor Rotating Spike via Time-Accurate Simulation", Journal of Propulsion and Power, 2009. <1%
Publication

---

38 A. Habibi. "Multiscale modeling of turbulent combustion and NOx emission in steam crackers", AIChE Journal, 09/2007 <1%
Publication

---

39 Du, L., A. Berson, and R. G. Dominy. "Aerofoil behaviour at high angles of attack and at Reynolds numbers appropriate for small wind turbines", Proceedings of the Institution of Mechanical Engineers Part C Journal of Mechanical Engineering Science, 2014. <1%
Publication

---

40 Seung-Hwan Yu, Kyoung-Sik Bang, Ju-Chan Lee, Woo-Seok Choi. "Flow characteristics inside a single basket containing a nuclear fuel assembly", Annals of Nuclear Energy, 2018 <1%
Publication

41	Aircraft Engineering and Aerospace Technology, Volume 81, Issue 5 (2009-10-02) Publication	<1%
42	Song, Yin, and Chunwei Gu. "Effects of Curvature Continuity of Compressor Blade Profiles on Their Performances", Volume 2A Turbomachinery, 2014. Publication	<1%
43	Du, Y.. "Coherent structure in flow over a slitted bluff body", Communications in Nonlinear Science and Numerical Simulation, 200606 Publication	<1%
44	Khan, Rafi Ullah. "Vacuum gas carburizing fate of hydrocarbons", Universität Karlsruhe, 2008. Publication	<1%
45	Yang, I.H.. "A three-dimensional simulation of a hydrocyclone for the sludge separation in water purifying plants and comparison with experimental data", Minerals Engineering, 200405 Publication	<1%
46	JayaKrishna Devanuri, Nesrin Ozalp. "Response to the comments made by Khalid M. Saqr on our paper titled “CFD analysis on the influence of helical carving in a vortex flow solar reactor”, Int. J. Hydrogen Energ. 2010: 35, 6248–6260.", International Journal of Hydrogen	<1%

Energy, 2011
Publication

47 Mansour, M. K.. "Effect of natural convection on conjugate heat transfer characteristics in liquid minichannel during phase change material melting", Proceedings of the Institution of Mechanical Engineers Part C Journal of Mechanical Engineering Science, 2014.
Publication

<1%

Exclude quotes	Off	Exclude matches	Off
Exclude bibliography	On		